INL/EXT-19-53248
Revision 0

Light Water Reactor Sustainability Program

Vibration-based Techniques for Concrete Structural-health Monitoring

March 2019

U.S. Department of Energy
Office of Nuclear Energy

INL/EXT-19-53248

Light Water Reactor Sustainability Program

Vibration-based Techniques for Concrete Structural-health Monitoring

Sarah Miele, Yanqing Bao, Pranav Karve,
Sankaran Mahadevan, Vivek Agarwal, Eric Giannini,
and Jinying Zhu

March 2019

Idaho National Laboratory
Idaho Falls, Idaho 83415

Vanderbilt University
Nashville, Tennessee 37235

Prepared for the
U.S. Department of Energy
Office of Nuclear Energy
Under DOE Idaho Operations Office
Contract DE-AC07-05ID14517

ABSTRACT

Assessment and management of aging concrete structures in nuclear power plants require a more systematic and automated approach than simple reliance on existing-code margins of safety. The current fleet of nuclear power plants perform time-based periodic inspection of concrete structures to understand the condition of the structure based on nondestructive evaluation heterogeneous measurements and then an actionable information regarding structural integrity is generated. This information is used to support execution of the aging management plan.

The objectives of this ongoing research project focus on health monitoring and data analytics of concrete slabs containing reactive aggregates and, thus, subject to degradation due to alkali-silica reaction (ASR). A controlled concrete slab with four pockets of reactive aggregates (pure silica, and reactive aggregates from three different quarries) was cast at Vanderbilt University and cured in representative conditions to accelerate degradation due to ASR. A set of four concrete samples were also cast and cured at the University of Alabama for ASR testing. Of these four samples, two slabs contained reactive aggregates while the other two had non-reactive aggregate counterparts mixed throughout the samples. Four additional slabs were cast and cured at the University of Nebraska–Lincoln. Of these four samples, one contained non-reactive aggregates and no reinforcement, one contained reactive aggregates and no reinforcement, one contained reactive aggregates and rebar reinforcement in one direction, and the last contained reactive aggregates and reinforcement in two directions. Single- and dual-frequency tests were used on these slabs to locate ASR damage within the specimens containing reactive aggregates.

Vibration tests were conducted with different sensor and actuator configurations to facilitate damage detection and localization. The results from the data analysis of the dynamic testing on concrete slabs are discussed in detail in this report. Results for damage localization are dependent on multiple parameters used in the tests. This report investigates different methods of data fusion, including voting, raw averaging, damage index averaging, and Bayesian fusion.

EXECUTIVE SUMMARY

One challenge facing the current fleet of light water reactors in the United States is age-related degradation of their passive assets, including concrete, cables, piping, and the reactor pressure vessel. As reactors within the current fleet of nuclear power plants (NPPs) continue to operate for 60 years or more, it is important to understand the current and the future condition of passive assets under different operating conditions that would support cost-effective operational and maintenance decisions. To ensure safe, economical, and reliable long-term operation of the current fleet, the U.S. Department of Energy's Office of Nuclear Energy funds the Light Water Reactor Sustainability Program. The goal of the Plant Modernization Pathway with the Program is to extend life and improve performance of existing fleet through modernized technologies and improved processes for plant operation and power generation.

One among many different passive assets of interest in NPPs, reinforced concrete structures are investigated in this research project. These concrete structures are affected by a variety of degradation mechanisms that are related to chemical, physical, and mechanical causes and to irradiation. Age-related degradation of concrete results in gradual microstructural changes (e.g., slow hydration, crystallization of amorphous constituents, and reactions between cement paste and aggregates). The structural integrity of concrete structures is evaluated via time-based periodic inspections based on heterogeneous nondestructive examination measurements and then an actionable information is generated to support aging management plan. The current time-based periodic inspection approach is performed by skilled workers at specific location. This is a time-consuming, inefficient, and cost prohibitive approach.

The purpose of structural health monitoring of concrete is to replace the time-based periodic inspection approach with condition-based inspection approach. The structural health monitoring of concrete will perform automated diagnosis of the current condition of a structure using advanced sensor technologies and prognose the future condition using data analytics and machine learning techniques. This will provide high-confidence actionable information regarding structural integrity and reliability. Vanderbilt University, in collaboration with Idaho National Laboratory and Oak Ridge National Laboratory, is investigating and enhancing a probabilistic framework for structural health monitoring and managing the condition of aging concrete structures in NPPs. This integrated framework includes four elements: (1) monitoring, (2) data analytics, (3) uncertainty quantification, and (4) prognosis.

The objective of this research is to obtain degradation data for concrete structures from a series of experiments conducted under controlled laboratory conditions. This report focuses on concrete degradation caused by alkali-silica reaction (ASR). Concrete specimens are prepared to develop accelerated ASR degradation in a laboratory setting. Different monitoring techniques, which include thermography, mechanical-deformation measurements, nonlinear impact resonance-acoustic spectroscopy, and vibro-acoustic modulation (VAM), were previously used to detect the damage caused by ASR on concrete slabs cured at Vanderbilt University, and were documented in an earlier report.

The current report focuses on damage localization using vibration-based techniques and investigates the effect of different characteristics of single- and dual-frequency vibration tests on the damage localization results. The report also discusses

the significance of optimal sensor placement and selection of experimental parameters, and their impact on overall accuracy of diagnosis and prognosis. Some of the notable outcomes reported in this report are as follows:

1. Single- and dual-frequency vibration testing performed on two sets of concrete slabs without reinforcement. These include, (1) 24 × 24 × 6 in. concrete slab cast at Vanderbilt University with four different types of reactive aggregates placed at specific locations and aggressively cured to produce accelerated ASR degradation; and (2) 12 × 24 × 12 in. concrete slabs cast and cured at University of Alabama with different reactive and non-reactive aggregates mixed throughout the samples.
2. Both single- and dual-frequency techniques detected and localized the damage in the medium-sized concrete slabs from both Vanderbilt University and Alabama University.
3. The vibration test results were fused using voting, averaging, and Bayesian techniques.
4. Single- and dual-frequency vibration tests show consistent results for damage localization in the Alabama specimens compared to the Vanderbilt specimen.
5. Detection and localization of ASR was carried out in four 12 × 24 × 12 in. concrete slabs, cast and cured at the University of Nebraska–Lincoln. Of the four samples, one contained non-reactive aggregates and no reinforcement, one contained reactive aggregates and no reinforcement, one contained reactive aggregates and rebar reinforcement in one direction, and the last contained reactive aggregates and reinforcement in two directions.

The experiments described in this milestone report are focused on concrete structural monitoring measurements and data analytics. The damage and uncertainty quantification methodology will support continuous assessment of concrete performance and enhance the prognostics and health management framework. In addition, the finding in this report lay the foundation for implementation strategy of autonomous monitoring of concrete structures using vibration-based techniques.

ACKNOWLEDGMENTS

This report was made possible through funding by the U.S. Department of Energy's Light Water Reactor Sustainability Program. We are grateful to Alison Hahn of the U.S. Department of Energy and Bruce Hallbert and Craig A. Primer at Idaho National Laboratory for championing this effort

CONTENTS

FIGURES

TABLES

ACRONYMS

ASR	alkali-silica reaction
EPRI	Electric Power Research Institute
FFT	fast Fourier transform
LS	linear spectrum
NDE	nondestructive examination
NIRAS	nonlinear impact resonance-acoustic spectroscopy
NPP	nuclear power plant
NRC	Nuclear Regulatory Commission
PMF	probability mass function
PSD	power spectral density
RBF	radial basis function (kernel)
SBSum	sideband sum
SHM	structural health monitoring
SV	single vector
VAM	vibro-acoustic modulation

Vibration-based Techniques for Concrete Structural-health Monitoring

1. INTRODUCTION

The majority of existing nuclear power plants (NPPs) continue to operate beyond their initial licensed life expectancy. The passive structures, systems, and components of NPPs as they continue to operate suffer deterioration that affects structural integrity and performance. Monitoring the condition of these elements of an NPP is essential for ensuring that their conditions meet performance and safety requirements over the entire expected plant lifespan. This project focuses on concrete structures in NPPs. The concrete structures are grouped into the following categories: (1) primary containment, (2) containment internal structures, (3) secondary containment/reactor buildings, and (4) other structures, such as used fuel pools, dry storage casks, and cooling towers. These concrete structures are affected by a variety of chemical, physical, and mechanical degradation mechanisms, such as alkali-silica reaction (ASR), chloride penetration, sulfate attack, carbonation, freeze-thaw cycles, shrinkage, and mechanical loading (Naus 2007). The age-related deterioration of concrete results in continuing microstructural changes (e.g., slow hydration, crystallization of amorphous constituents, and reactions between cement paste and aggregates). Therefore, it is important that changes over long periods of time be measured and monitored, and that their impacts on the integrity of the components be analyzed to best support long-term operations and maintenance decisions of existing fleet of nuclear reactors.

Structural health monitoring (SHM) can produce actionable information regarding structural integrity that, when conveyed to the decision maker, enables risk management with respect to structural integrity and performance. The SHM methods and technologies include assessment of critical measurements, monitoring, and analysis of aging concrete structures under different operating conditions. In addition to data from the specific system being monitored, information may also be available for similar or nominally identical systems in an operational NPP fleet, as well as legacy systems. Therefore, to take advantage of this valuable information Christensen (1990) suggested that assessment and management of aging concrete structures in NPPs require a more systematic and dynamic approach than simple reliance on existing code margins of safety.

Through the Light Water Reactor Sustainability Program, national laboratories (Idaho National Laboratory and Oak Ridge National Laboratory) and universities (Vanderbilt University, University of Nebraska-Lincoln, University of Alabama, University of South Carolina, and Georgia Tech University) have been investigating concrete SHM techniques. In this report, the focus is on the collaboration between national laboratories and Vanderbilt University in researching concrete SHM techniques in accordance with the framework discussed in Mahadevan et al. (2014). The goal of this research is to enable plant operators to make risk-informed decisions on structural integrity, remaining useful life, and performance of concrete structures across the NPP fleet. The project's long-term research objective is to produce actionable information regarding structural integrity that is individualized for a structure of interest and its performance goals. In addition, the project supports the research objectives of three pathways under the Light Water Reactor Sustainability Program (i.e., the Plant Modernization Pathway; the Materials Research Pathway; and the Risk-Informed System Analysis Pathway).

The framework investigates concrete structure degradation by integrating the following technical elements: (1) health condition monitoring, (2) data analytics, (3) uncertainty quantification, and (4) prognosis. For details on each element of the framework, refer to Mahadevan et al. (2014). The framework will help plant operators to make risk-informed decisions on structural integrity, remaining useful life, and concrete structure performance. The demonstration performed at Vanderbilt University using various techniques to assess ASR degradation in controlled concrete specimens was reported in Mahadevan et al. (2016, 2017).

The objective of this report is to examine the use of vibration-based techniques in informing the prognostics and health management (PHM) framework. Experiments were conducted at Vanderbilt to provide sufficient degradation data in support of the PHM framework (Mahadevan et al. 2014; Mahadevan et al. 2016) used to examine and forecast the condition of aging concrete structures in NPPs. Within this experimental campaign, multiple concrete slab samples were exposed to different accelerated aging conditions in a laboratory to ensure formation of ASR gel within an observable time frame. These concrete samples differ in size and in the types of embedded aggregates incorporated. Single- and dual-frequency tests were used to detect and assess the ASR-induced damage in these concrete samples over an extended period of time.

The technical background, experimental setting, data processing, significant results, technical findings, and conclusion are included in the remainder of the report is organized as follows:

- Section 2 discusses the technical basics of ASR development and the vibration-based techniques used to assess the effects of ASR on the integrity of multiple concrete samples.
- Section 2.2 details the results of single frequency testing for damage detection and localization.
- Different data fusion techniques for dual frequency tests on concrete specimens are presented in Section 2.3.
- Section 6 discusses four reinforced concrete specimens cast at the University of Nebraska–Lincoln with reactive aggregates that contained varied amounts of steel reinforcement. A description of dual frequency testing on these specimens and results are also displayed in this section.
- Research summary and future work are discussed in Section 7.

2. TECHNICAL BACKGROUND

2.1 Alkali-silica Reaction Damage

ASR is a reaction in concrete between the alkali hydroxides (K^+ and Na^+) in the pore solution and the reactive non-crystalline (amorphous) silica (S^{2+}) found in many common aggregates, given sufficient moisture. This reaction occurs over time and causes the expansion of the altered aggregate by the formation of a swelling gel of calcium silicate hydrate (C-S-H). Reactive silica is mainly provided by reactive aggregates and the alkalis by the cement clinker. ASR swelling results from the relative volume increase between the product and reactant phases involved in the chemical reaction. First, the products expand in pores and microcracks of the cementitious matrix. Once this free expansion space is filled, the swelling is restrained, and the product phases exert local pressure on the surrounding concrete skeleton (Ulm 2000). Figure 1 depicts the mechanism of ASR (Kreitman 2011).

With water presence, the ASR gel increases in volume and exerts an expansive pressure inside the material, causing spalling micro-to-macro cracks (due to nonhomogeneous swelling related to non-uniform moisture distribution). As a result, ASR reduces the stiffness and tensile strength of concrete because these properties are particularly sensitive to microcracking. ASR can also cause serious cracking in concrete, resulting in critical structural problems that can even force the demolition of a particular structure. The serviceability of concrete structures includes resistance to excessive deflections, as well as a host of other durability concerns that can shorten the service life of a structure. Large surface cracks and deep penetration of open-surface cracks promote ingress of moisture and any dissolved aggressive agents, such as chlorides. Additionally, the loss of concrete stiffness and potential for reinforcement yield are concerns for concrete-deflection capabilities.

ASR is a complex chemical phenomenon, the rate and extent of which depend on a number of material and environmental parameters for which the interactions among parameters is not fully understood. This critical nature of ASR on premature concrete deterioration requires the quantitative assessment of ASR

structural effects during service life (both in time and space). In particular, a combined experimental modeling investigation method is required to evaluate the impact of ASR on the dimensional stability of concrete structures. Although ASR has been identified as a cause of deterioration of numerous concrete structures, and research has yielded some understanding of the mechanism of the reaction, the structural effects of ASR and how best to assess the extent of damage to existing structures remain major topics of ongoing research. This is because the expansion and cracking patterns—the most obvious sign of distress—caused by ASR affect both the concrete and the reinforcing steel, but similar crack patterns can also be produced by other distress mechanisms (i.e., drying shrinkage and sulfate attack).

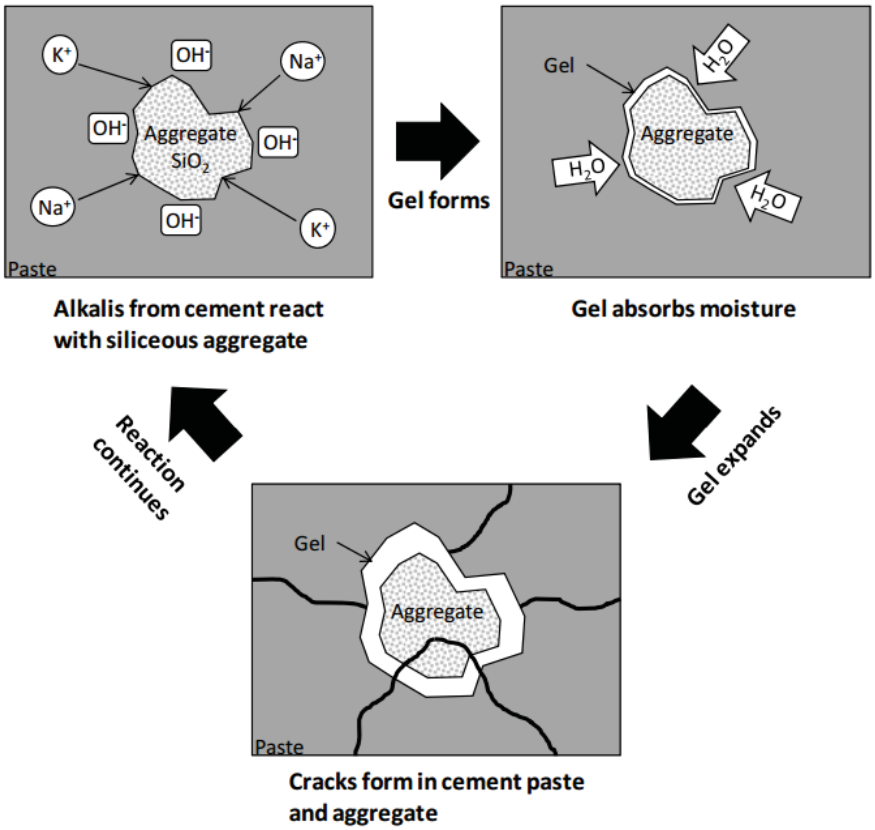

Figure 1. Mechanism of ASR (Kreitman 2011).

In the nuclear industry, a scoping study of ASR in concrete is performed to support future activities that include evaluating the effects of ASR on structural capacity. From a safety perspective, the remaining capacity of a structure exhibiting distress due to ASR is an important factor in operational and maintenance management decisions. This is a challenging task for various reasons. First, the extent of the degradation will vary throughout the element as a function of the moisture content and of the degree of restraint provided by steel reinforcement. Also, predicting the properties of the concrete using certain testing results taken from the structure may be difficult because the size of the defects caused by ASR may be large compared to a small structure, such as the cylinder (resulting in anomalously low tested strength), but the defects are small compared to the larger structure (suggesting there may be sufficient capacity). In addition, there is no reliable nondestructive means of estimating the degree of the reaction in an existing concrete structure.

ASR can potentially affect concrete properties and performance characteristics, such as compressive strength, the modulus of elasticity, flexural stiffness, shear strength, and tensile strength (Agarwal et al 2015). ASR can also impact material properties, but the structural performance of concrete elements depends on whether or not the concrete is unconfined or confined within reinforcing bars. Concrete core

testing was conducted at Seabrook Station Nuclear Power Plant in February 2011 as part of a license-renewal submission (NextEra Energy Seabrook 2012). These tests confirmed the presence of ASR-induced cracks in various structures within the plant and reduced modulus, to some extent. The impact of reduced modulus on ASR-affected structures was evaluated. This evaluation found that the overall structure integrity was still within the strength requirements.

2.2 Concrete Specimens

Monitoring techniques are studied using concrete samples constructed and cured in the laboratory. These include (1) a concrete slab (without reinforcement) with known pockets of reactive aggregate cast and cured at Vanderbilt University, in Nashville, Tennessee; (2) two plain concrete blocks (without reinforcement) with reactive aggregate and two plain concrete blocks with non-reactive aggregates cast and cured at the University of Alabama in Tuscaloosa, Alabama; and (3) four concrete blocks with reactive aggregates and different amounts of steel reinforcement cast and cured at the University of Nebraska–Lincoln.

2.2.1 Plain Concrete Slab at Vanderbilt University

A medium-sized concrete slab of dimensions of 2 ft × 2 ft × 6 in. was cast on December 21, 2015 and cured at Vanderbilt University. The details of the casting and curing process of this specimen are discussed in detail in a report by Mahadevan et al. (2016). Figure 2 shows an image of the slab immediately after the mold was removed.

Figure 2. 2 ft × 2 ft × 6 in. dimension concrete slab (Vanderbilt University).

Four types of aggregate were placed in pockets at a depth of 3 in. in the four quadrants of the slab (Figure 3). The aggregates were placed in pockets instead of being dispersed throughout the slab so that the reactivity of each aggregate can be determined independently. Additionally, since the locations of the pockets of aggregate are known, this information was used to validate the localization of ASR from vibration-based tests. The four types of aggregates used are as follows:

1. Pure silica powder from local ceramic shop
2. Coarse aggregate from Maine, donated by the University of Alabama
3. Coarse aggregate from New Mexico, donated by the University of Alabama
4. Coarse aggregate from a quarry in Ontario, Canada, donated by the Ontario Ministry of Transportation.

In October 2016, the first visual evidence of degradation due to ASR was observed. Since then, degradation-related damage became increasingly pronounced. Hairline cracks were observed on the

surface of the slab, and later, an ASR-gel effluent and whitish powder seeped out of the slab. In Figure 3, the red squares identify the locations where seepage of ASR-gel effluent was observed on the sides of the slab. The seepage corresponding to locations marked in red squares Figure 3 is shown in Figure 4 and Figure 5, respectively.

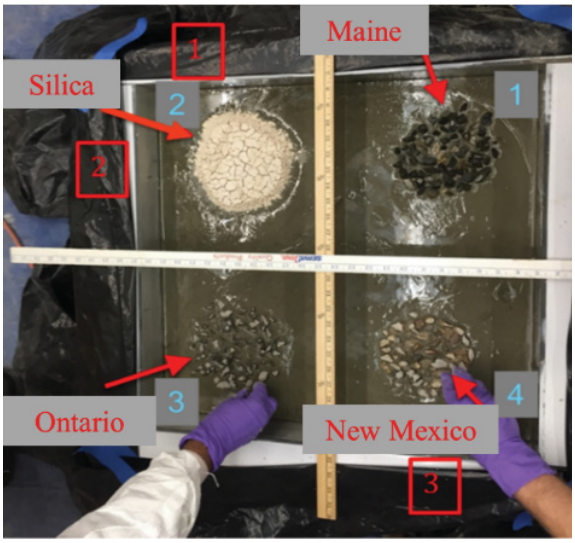

Figure 3. Pockets of aggregate in the slab during casting with red squares identifying visually observed cracks and effluence on the side of the slab.

Figure 4. Damage Location 1: cracking and powder effluence.

Figure 5. Damage Location 2: clear gel effluence.

Figure 6. Damage Location 3: cracking and powder effluence.

2.2.2 Plain Concrete Specimens from the University of Alabama

Four plain concrete blocks of dimensions of 2 × 1 × 1 ft^3 were cast and cured in accelerating conditions at the University of Alabama (Figure 7). Unlike the Vanderbilt specimen in which known pockets of aggregates were placed in the cement paste, the Alabama specimens used conventional concrete mixtures prepared in a rotating drum mixer. The aggregates were distributed throughout the blocks. All four specimens contained 25 mm coarse aggregates known to be susceptible to ASR (i.e., reactive) combined with a non-reactive crushed dolomite/calcite fine aggregate from Calera, Alabama. Two specimens contained a reactive river gravel coarse aggregate from Colorado and the other two specimens contained a reactive crushed green schist from North Carolina. All four specimens contained a low-alkali cement (0.46% Na_2O_{eq}), while two (one for each reactive aggregate) contained added sodium hydroxide (NaOH) to boost the alkali loading to 5.25 kg/m^3 to accelerate ASR. The alkali loading of the two specimens without NaOH was 1.61 kg/m^3. Mixture proportions can be found in Table 1. The specimens were instrumented with embedded targets for measuring expansion from ASR using a demountable mechanical strain gauge. Initial expansion measurements were taken following a minimum 48-hour moist cure in a 23°C temperature-controlled room. Following initial expansion measurements, specimens were placed in an environmental chamber maintained at 38°C and >98% relative humidity. This conditioning and monitoring process was continued for 466 to 504 days after casting. At this time, final expansion measurements were obtained, and the specimens were transferred to Vanderbilt University.

Table 1 also shows the final average expansion measured for each specimen. Based on the measured expansion behavior, the boosted specimens will be referred to as reactive, and the unboosted specimens as non-reactive.

Table 1. Design mixture proportions and final average expansions for specimens prepared at The University of Alabama (proportions for saturated-surface dry aggregates).

Component	Colorado Specimen kg/m^3	North Carolina Specimen kg/m^3
Coarse Aggregate	1138	1152
Fine Aggregate	711	749
Type II Cement	350	350
w/cm	0.50	0.50
Final Expansion, Boosted	+0.178%	+0.197%
Final Expansion, Unboosted	-0.022%	-0.022%

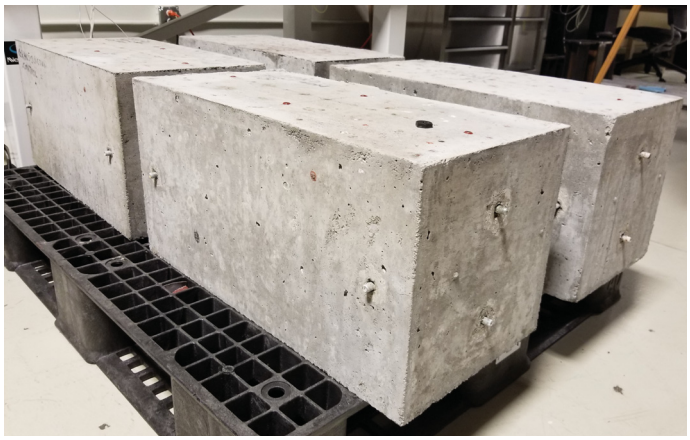

Figure 7. Two reactive and two corresponding non-reactive (control) specimens at the University of Alabama.

2.2.3 Reinforced Concrete Specimens from the University of Nebraska-Lincoln

Four concrete blocks of dimensions of 2 x 1 x 1 ft^3 were cast and cured in accelerating conditions at The University of Nebraska-Lincoln, Omaha (Figure 8). Similar to the Alabama samples, the Nebraska specimens used conventional concrete mixtures prepared in a rotating drum mixer. The aggregates were distributed throughout the blocks. All four specimens contained 25 mm coarse aggregates known to be susceptible to ASR (reactive) combined with a non-reactive crushed dolomite/calcite fine aggregate. All four specimens contained a reactive crushed green schist from North Carolina. All four specimens contained a low-alkali cement (0.46% Na_2O_{eq}), while three contained added sodium hydroxide (NaOH) to boost the alkali loading to 5.25 kg/m^3 to accelerate ASR. Here, the three samples treated with NaOH will be referred as reactive and the sample not treated with NaOH will be referred to as non-reactive. Two specimens were reinforced with rebar, one specimen has rebar only in one direction while another specimen has rebar in two directions. The Nebraska concrete specimens are labeled as, Nebraska - Control, Nebraska – non-reinforced, Nebraska – reinforced 1-D, and Nebraska – reinforced 2-D.

Figure 8. Specimen cast at University of Nebraska-Lincoln.

2.3 Vibration Testing

Multiple types of SHM technique have been studied for detecting ASR damage in concrete structures. Earlier reports by Mahadevan et al. (2016 and 2017) have studied various techniques and found them to be useful in detecting damage. Two vibration-based testing techniques showed particular promise in damage localization and were investigated further. A brief overview of two vibration-based techniques is given below.

2.3.1 Single-frequency Vibration Testing

The tests employed a waveform generator, a wave amplifier, a National Instruments data acquisition (NI-DAQ) system, an actuator, and single axis accelerometers. The waveform generator was used to tune parameters of the waveform. The actuator and the nine accelerometers were mounted on the top surface of the sample at the locations shown in Figure 10.

The experiments used sinusoidal waveforms at 5000 Hz and a sweep waveform (linearly swept from 200 to 5000 Hz in 1 second). The frequencies were chosen based on the lowest effective frequency of the actuator and the highest sampling frequency in the NI-DAQ system. Due to limitations of the accelerometer range, the amplitude of the waveform was set to be constantly at 1000 mV for all the tests. In each pitch-catch test, the signal of a specific waveform (either pure sinusoid or swept waveform) generated by the actuator was received by the nine accelerometers at different locations, and each test lasted for 1.5 seconds. Overall, 100 tests were carried out with each of the waveform settings for both the intact sample and the damaged sample.

2.3.1.1 Tests on Alabama Samples

In this section, we carried out tests on the four Alabama samples of dimensions as in Figure 9 with ASR-reactive aggregates from North Carolina and Colorado. We have one control sample and one reactive sample for each aggregate design. The reactive samples were cured in alkali and humid condition for over a year. The presence of ASR was first detected using deformation measurements (i.e., expansions of the Alabama reactive samples with North Carolina and Colorado aggregates).

The locations of the accelerometers and the actuator for the single-frequency tests are shown in Figure 10. For the sake of illustration, for single-frequency experiment, we placed accelerometers on one half of the sample and performed 100 tests for each of the specific settings. Each test lasted for 1.5 seconds duration.

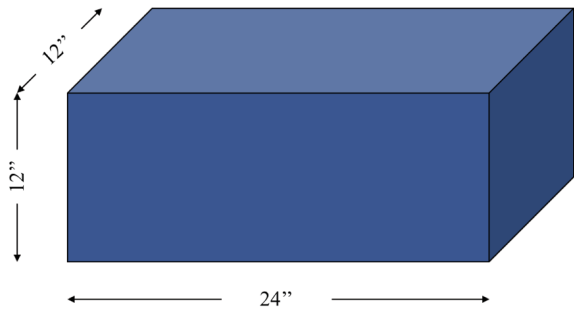

Figure 9. Dimensions of the Alabama samples.

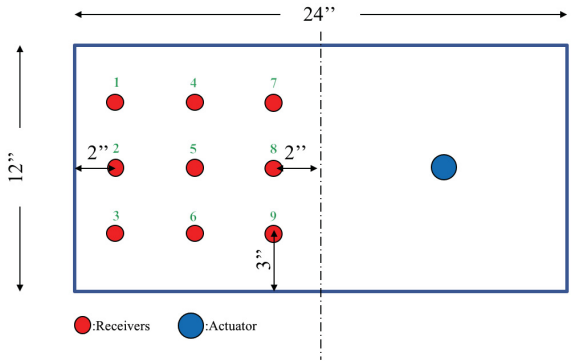

Figure 10. Locations of the accelerometers and the waveform actuators.

2.3.1.2 Theoretical Background of Proposed SVD-based Feature and K-Factor

Data collected from the experiments, after preprocessing, are represented in a matrix $X = [x_1, x_2, \dots, x_n]$ where each x_i represents a column vector of data collected in test number i. Then we perform singular value decomposition (SVD) as $X = USV^T$. Because the columns of U form an orthonormal basis, we reconstruct the signal with the last several left singular vectors, from k to n, which can be done practically by setting the diagonal values of S to be zeros from 1 to $k-1$, to get S^*. The reconstructed signals are calculated as

$$X^* = [x_1^*, x_2^*, \dots, x_n^*] = US^*V^T \tag{1}$$

Each x_i^* is a reconstructed signal using few of the last several left singular vectors. Utilizing the reconstructed signal x_i^*, a damage-sensitive feature is calculated using the formula

$$E_i = \sum_{j=1}^{n} {x_{i,j}^*}^2 \tag{2}$$

where E_i represents the energy of the reconstructed signal x_i^*, and $x_{i,j}^*$ represents the value of the reconstructed signal at time step j. Utilizing the calculated damage-sensitive feature values from different stages of the concrete sample as they cured and developed ASR degradation, we performed damage detection by setting a threshold based on the feature values. The damage-sensitive feature (Equation (2)) is able to differentiate the data collected on damaged samples from the data collected on intact samples, as presented in Section 3.2.

The next step is to identify the location of the damage by using data from multiple accelerometer locations. The assumption here is that the internal damage or crack will cause a discontinuity in the material, especially for acoustic wave transmission. Therefore, if we set the waveform at the actuator to be a sinusoid, the acquired signals at accelerometers mounted at different locations will be differently affected by the damage and deviate from the sinusoid at different levels. The amount of deviation will be affected by the location of the accelerometer, with the highest deviation observed when the accelerometer is mounted closest to the region where damage is present. As we acquire time series data from the accelerometers at different locations, we calculate the corresponding K-factor for each of the locations. After that, by comparing the relative values of the K-factors, we will be able to identify the possible locations of the damaged zones.

For each of the sinusoidal input pitch-catch tests, the K-factor (crest factor) can be calculated as

$$K_i = x_{i_{peak}} * rms\,(x_i) \tag{3}$$

After the calculation of the K-factors from the data collected by the accelerometers at each location, damage localization can be performed by comparing the K values. There are several possible methods to determine the damage locations, such as direct observation, maximum-value position, and use of

unsupervised learning algorithms. In this study, we selected two methods, direct observation and *k*-means clustering, (an unsupervised learning method). Other metrics might be found suitable for different applications but are not explored here.

2.3.2 Dual-frequency Testing (Vibro-acoustic Modulation)

Vibro-acoustic modulation (VAM), also known as nonlinear wave modulation spectroscopy, is an nondestructive evaluation (NDE) technique that relies on detecting dynamic signature of nonlinear structural behavior as the primary indicator of damage. Specifically, VAM aims at detection of modulation of a higher frequency by a lower frequency caused by delamination or cracks in structural components. The utility of VAM for detecting debonding flaws and cracks in composites, metals, as well as ASR-induced cracks in concrete (Chen et al. 2008, Chen et al. 2009) has been demonstrated in the past.

In a VAM technique, the structural component of interest is excited simultaneously using a combination of two signals of specific frequencies, and the dynamic response is measured at various locations using acoustic sensors (accelerometers). The low-frequency input is termed the "pump," and the high-frequency input is termed the "probe" (Kim et al. 2014). The geometric or material nonlinearity in the form of variable contact area or nonlinear adhesive bond at the surfaces of a crack or a delamination causes modulation of the probing frequency (f_{pr}) by the pumping frequency (f_{pu}). This modulation, and hence, the presence of the flaw can be seen in the frequency spectra of measured response as peaks of higher magnitude (sidebands) around the probe frequency. The interaction of these signals at different frequencies is used to understand the nonlinear stress-strain relationship in the structure of interest. Most of the previous work on VAM tests has focused on *detection* of damage based on the presence of side bands in the spectrum of dynamics response of the structure. Recently, Singh et al. (2017) showed that a VAM test can be used for damage *localization* or damage mapping. They hypothesized that the effect of (geometric or material) nonlinearities is pronounced near the location of the flaw; hereafter, the relative magnitude of a sidebands-based damage index may enable localization of the flaw. That is, if the spatial distribution showing the variation of the damage index is obtained using a sensor grid, the damage is located in the neighborhood of sensors exhibiting higher magnitude of the damage index. They tested their hypothesis using numerical simulations of VAM in delaminated composite plates. They studied damage indices based on various characteristics of spectrum of the dynamic response (magnitude of sidebands, probe frequency, pump frequency) of the plate and established the feasibility of VAM-based damage localization. Thus, the utility of the damage mapping scheme has been studied for homogeneous, anisotropic, thin-composite plates by performing numerical experiments. We remark that thick, heterogeneous structural concrete components present significant challenges for VAM test setup, data analytics, and damage mapping.

VAM is a vibration-based method that utilizes signatures of nonlinear dynamic interactions on contact surfaces of cracks or delamination damage to detect and localize the damage. VAM tests were conducted on the medium-sized slab with reactive aggregate pockets at known locations (i.e., the Vanderbilt specimen), as well as on four concrete blocks cast using either reactive or non-reactive aggregates (for the Alabama slabs).

2.3.3 Vibro-acoustic Modulation Test Setup for Experimental Analysis

In laboratory experiments, we deliver the pump and probe excitations using piezo-stack actuators. We vary the locations of these actuators, as well as the frequencies at which they operate (i.e., the pump and probe frequencies). We measure the response of the structural component of interest using a finite number of accelerometers placed on the surface of the component. The relative magnitudes of sidebands at various accelerometer locations are used to map the damage (ASR-induced cracks) in the component. The performance of the VAM test depends on the values of parameters used, as well as on the methodology used for processing the data collected during a VAM test.

In these experiments, we used the first fundamental frequency of the slab as the f_{pu} (Table 2). We estimated the fundamental frequency of the structural component by conducting a hammer test. That is, we excited the structural component using an impact hammer and measured the acceleration at various locations using accelerometers. We computed the power spectral density (PSD) of the measured acceleration time series using the Welch's method (Welch 1967). The PSD shows multiple peaks that correspond to natural frequencies of the structure. The first and most prominent peak was noted to be the first modal frequency. For Vanderbilt's medium-sized slab, this value was 920 Hz. The frequency of 920 Hz was used as f_{pu} for this slab for all experiments. For the Alabama samples, 920 Hz was used as an arbitrarily low f_{pu}, in addition to the first modal frequencies for each sample. The modal frequencies for the all samples found using a hammer test are listed in Table 2.

Table 2. Experimental first modal frequency for each sample.

Slab Sample	Approximate First Modal Frequency (Hz)
Vanderbilt's Medium Slab	920
Alabama- North Carolina Reactive	1865
Alabama- North Carolina Control (non-reactive)	2390
Alabama- Colorado Reactive	1695
Alabama- Colorado Control (non-reactive)	2240

It has been reported in the literature that the probing frequency, f_{pr}, should be at least 10 to 20 times the pumping frequency (Singh et al., 2017). When the f_{pr} is N times the pumping frequency, it allows for the crack to open and close N times in a pumping cycle. Thus, the ratio between the pump and probe decides the opportunity (number of times per cycle of pumping vibrations) for modulation to occur. In accordance with these guidelines, probing frequencies ranging from 10 to 21 kHz were used in our experiments. The amplitude and location of the probing signal was also varied in different experiments.

In numerical studies the f_{pr} worked best for damage localization when it was 1/10th the amplitude of the f_{pu}. In general, this is true for our experiments. The acceleration spectra plots do not show this clearly because the ordinates of the spectra are multiplied by the square of the circular frequency. However, in linear spectra of displacements, the strength of the probing signal is always less than the strength of the pumping signal. In our experiments the pump and probe signal amplitudes were controlled by signal (function) generators. We used four amplitudes for the output voltage of the probing signal generator: 500, 250, 100, or 50 mV. The output voltage of the pumping signal generator was maintained at 500 mV. The pumping and probing signals were amplified by an amplifier and sent to the piezo-stack actuator. A constant amplification factor (+28 dB) was maintained for all tests.

A maximum of 21 accelerometers at a time are placed on the concrete specimen and connected to the data acquisition system. The locations of these accelerometers were varied for each experiment. The accelerometers had a sensitivity of 100 mV/g. In previous testing, we only used 12 accelerometers with a sensitivity of 10 mV/g.

2.3.4 Calculation of the Damage Index (Sideband Sum)

In laboratory experiments, multiple accelerometers were placed on concrete specimens cured in an aggressive environment (60ºC and 100% relative humidity) to encourage ASR. The slab was excited using pump and probe frequencies, and the time history of accelerations was recorded at different locations on the surface of the slab. The linear spectrum (LS) of the noisy acceleration-time history was computed using the Welch's method (Welch 1967) with zero overlap and a Nuttall-defined, 2048-point, four-term, symmetric, Blackman-Harris window (Nuttal 1981). LS of the acceleration-time history was computed from the PSD. The nonlinearity in the structural response, or the modulation of the f_{pr} by the

f_{pu}, is seen as sidebands around the f_{pr} ("peaks" in the LS at frequencies equal to ($f_{pr} \pm f_{pu}$). After computing the LS, the values of AmpS1 and AmpS2 (as shown in Figure 11) were used to calculate the sideband sum (denoted as SBSum). In this report, we discuss mapping of ASR-induced cracks based on the SBSum metric, SBSum = AmpS1 + AmpS2 (see Figure 11).

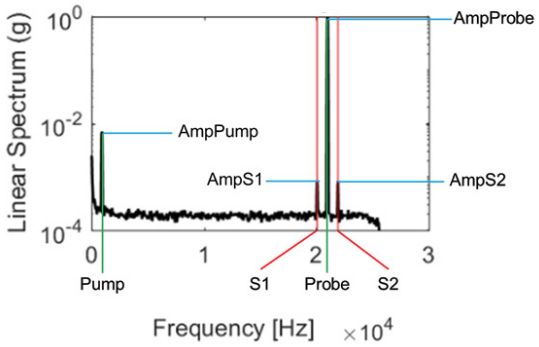

Figure 11. LS Plot for an accelerometer, labeled to show the values used in calculating SBSum. SBSum = AmpS1 + AmpS2.

2.3.5 Baseline adjustment and local peaks

The methodology for mapping damage using a sideband-based damage index has been demonstrated using numerical simulations (Singh et al. 2017). However, the various practical aspects of the methodology have not been studied in the past. For example, data collected in laboratory experiments contain noise and the LS in the neighborhood of the sidebands do not show near-zero amplitudes at all sensor locations. Thus, an automated sideband detection algorithm may identify the *ambient* LS values at ($f_{pr} \pm f_{pu}$) as sidebands. In processing the data, we conducted baseline adjustment and other sideband detection techniques. In baseline adjustment, we subtracted the average of the LS ordinates in the neighborhood of the sidebands from the sideband values calculated from the LS. An automated SBSum calculation process may also be misled by considering ordinates at given frequencies that are not peaks (hence, they do not indicate nonlinear structural behavior). To ensure that the values being used to calculate SBSum are physically meaningful sidebands, a method for finding local peaks in the data was implemented. In this method, it was first determined whether the sideband value for a given frequency was a local peak. Next, we checked whether the sideband was a maximum value within a 1000 Hz window, centered at the sideband frequency of interest. The ordinate value at a given frequency was selected as a sideband only if it satisfies both the conditions given above (Mahadevan et al. 2018).

3. SINGLE FREQUENCY VIBRATION TESTING RESULTS

This section displays results for damage detection and localization using the single frequency vibration testing technique. The tests were conducted for the Vanderbilt and Alabama specimens.

3.1 Vanderbilt Specimen

We carried out experiments, as described in Section 2.3, on the specimen cast at Vanderbilt University with a different type of ASR reactive aggregate in each quadrant. To obtain better resolution for the damage localization analysis, we divided the concrete block into two zones (as shown in Figure 12). To get better resolution of damage localization, each time, the accelerometers were mounted on the top surface of the concrete over one half of the slab. Because we already had visual confirmation of damage, we focused on the damage localization. As mentioned in Section 2, we carried out vibration tests with pure sinusoidal waves at 5000 Hz and calculated the corresponding K-factor for the data collected at

each of the accelerometers. We performed damage localization for each half individually and then merged interpretations from the two halves, to form an overall damage location estimation.

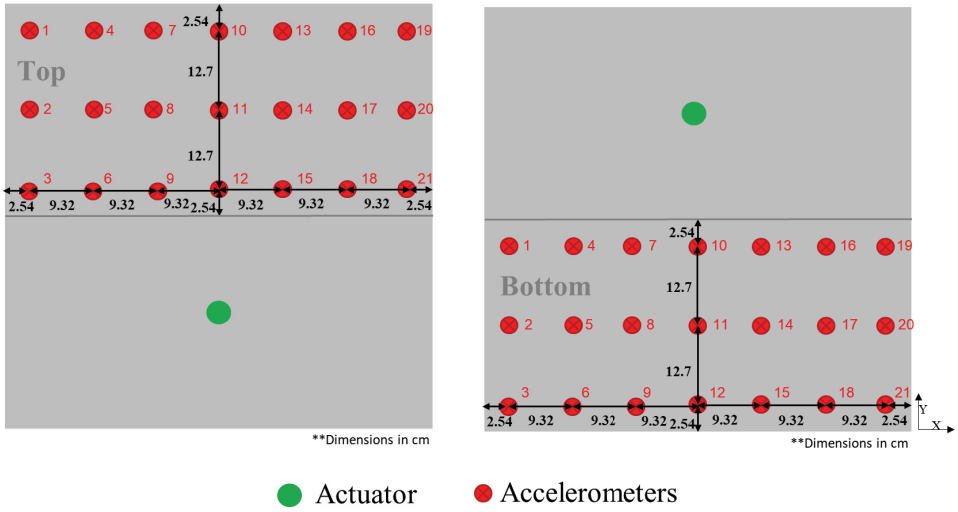

Figure 12. Locations of the accelerometers on one half.

Here we used two interpolation methods, spline and cubic schemes, to get a smooth estimation. In Figure 13, the red area refers to high K-factor values—i.e., is a more probably damaged location. As we proposed that the K-factor is a relative comparison metric, our method uses the relative values from the sensor arrays rather than the absolute values of the K-factors, the blue area refers to low K-factor values, suggesting least probably damaged location.

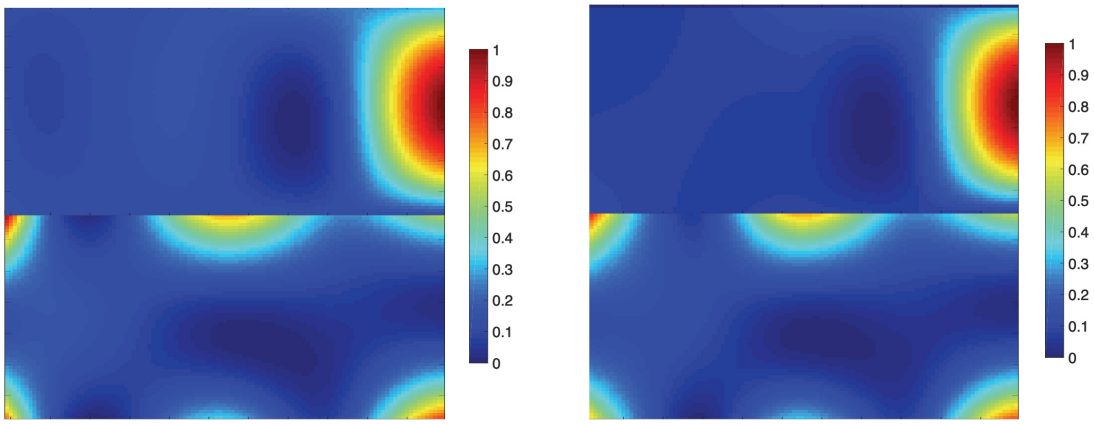

Figure 13. Damage localization using normalized K-factor values with spline interpolation (left) and cubic interpolation (right) for the Vanderbilt medium slab.

The Figure 13 shows that the top right quadrant had the most severe damage. The lower left and right edges also had minor damage. Meanwhile, a horizontal damage, maybe a crack, was indicated near the center of the top surface concrete. The results shown in Figure 13 are for cases where the actuator is outside the sensor array. Figure 14 shows an example of a result when the actuator was placed within the sensor array for the top half of the specimen.

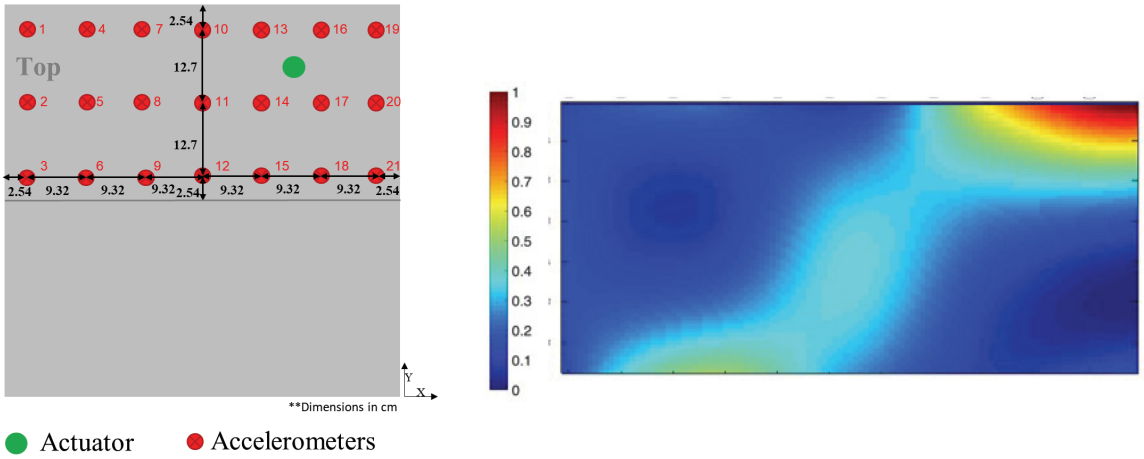

Figure 14. Damage map for an actuator within the sensor array for the top half of the Vanderbilt specimen.

3.2 Alabama Specimens

3.2.1 Damage Detection

The data sets of the control samples were divided into two subsets, 70% for damage-sensitive basis construction and 30% for validation. Then, all data points were projected on the created intact basis, as described in Section 2.3.1.2, and the damage-sensitive feature (energy) was computed based on the reconstructed the signal with the 21st to 50th singular values

The results are shown in Figure 15 and Figure 16. Blue plus signs represent the feature values for the 70% control samples; red plus signs represent the values for the reactive samples, and blue circles represent the values for the 30% control validation samples. It is seen that the feature values for the reactive samples were much lower than those for the control samples, and the differences were significant enough to make damage detection clear.

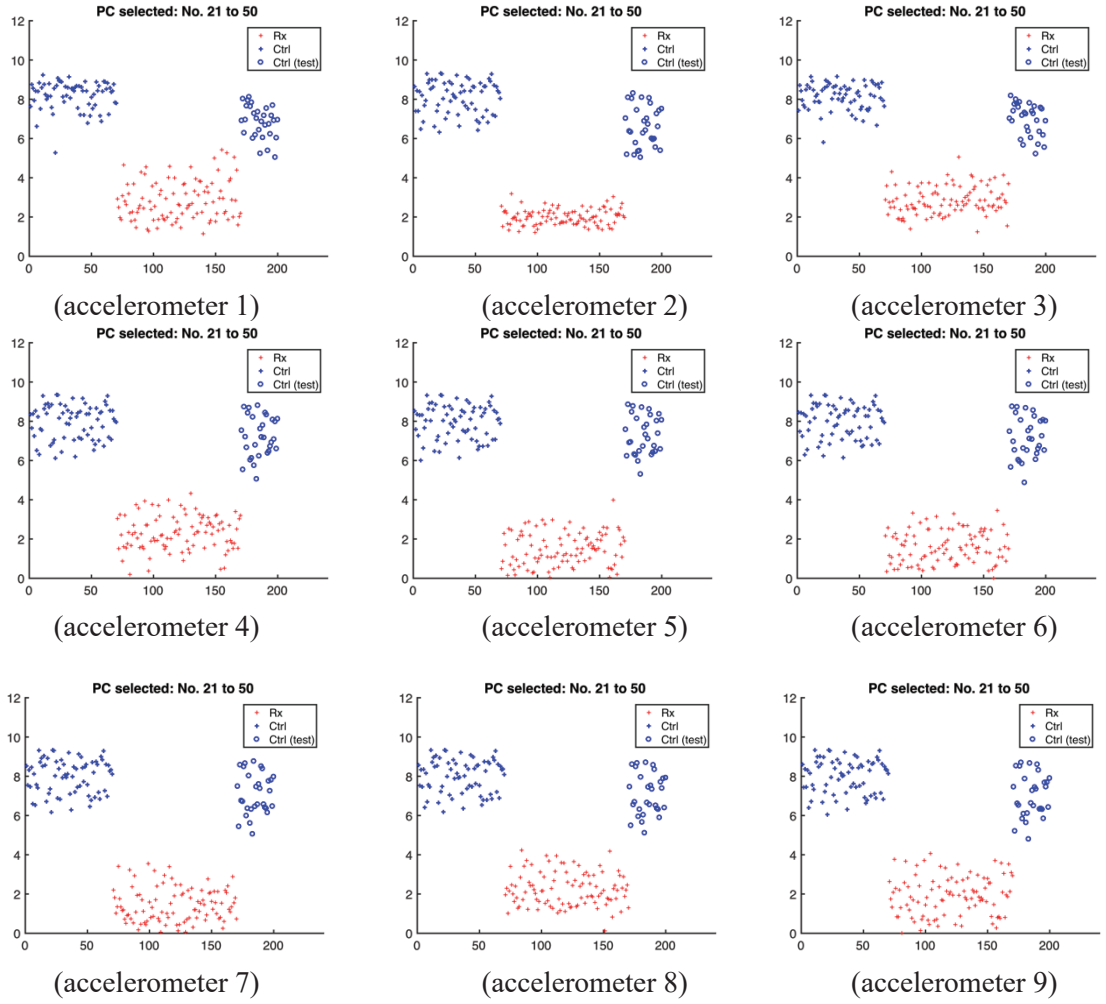

Figure 15. SVD-based features of Alabama samples with North Carolina aggregates (x-axis: dataset number; y-axis: SVD-based feature value). Blue – non-reactive aggregate; Red – reactive aggregate.

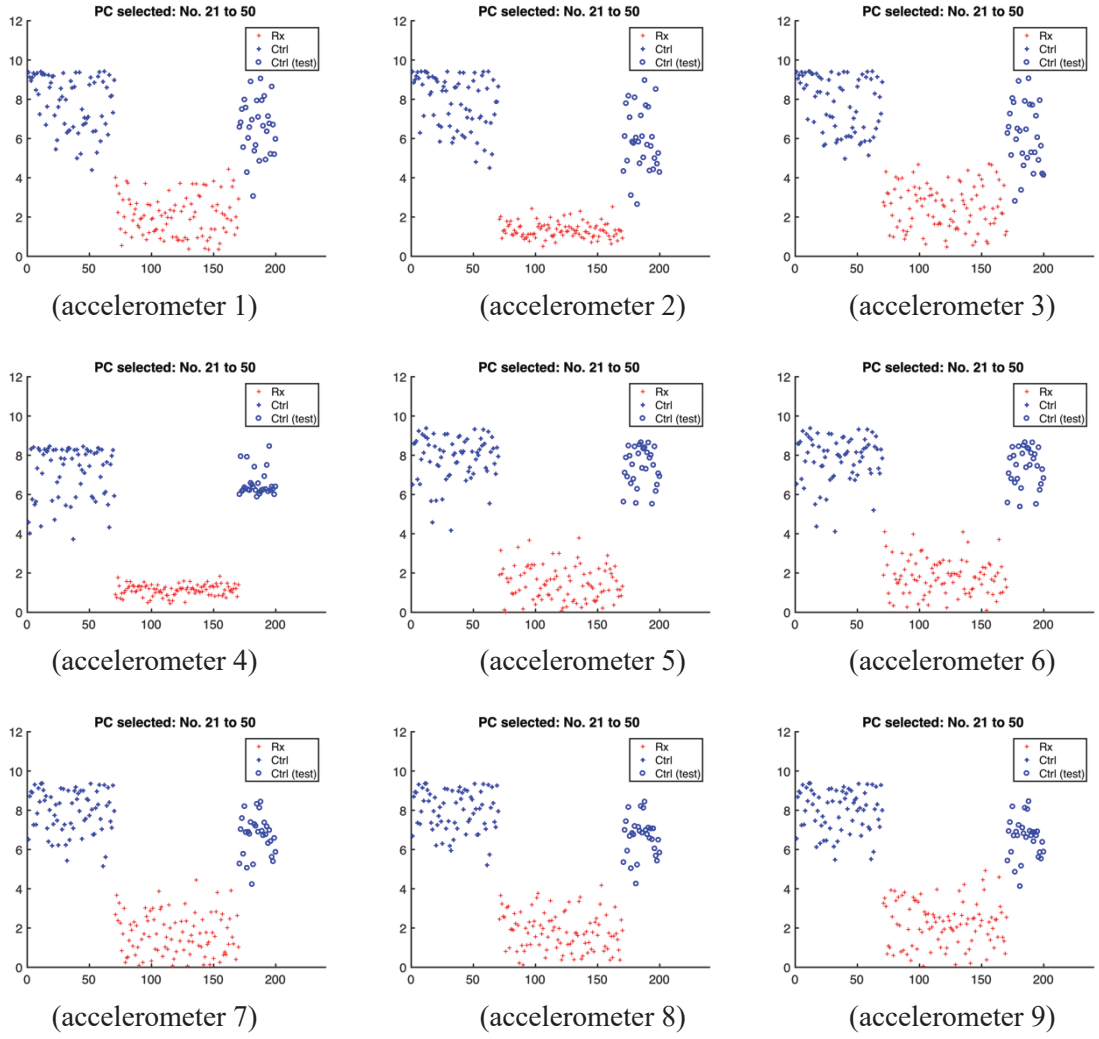

Figure 16. SVD-based features of Alabama samples with Colorado aggregates (x-axis: dataset number; y-axis: SVD-based feature value). Blue – non-reactive aggregate; Red – reactive aggregate.

3.2.2 Damage Localization

For damage localization, the sinusoidal data from intact specimen and degraded specimen are compared to compute the crest factors at each of the accelerometer locations. The assumption in using the crest factor is that higher values of the crest factors indicate more damage under that specific accelerometer. Since this process was a relative comparison, there could be multiple different metrics to make decisions. Here we illustrate two metrics: direct observation and *k*-means clustering.

The results of direct observation are shown in Figure 17 and Figure 18. For the of reactive Alabama samples with North Carolina Aggregates, the values of the crest factors from accelerometers 2, 3, 5, and 6 were much higher than from other accelerometers. Therefore, we could infer from the locations of accelerometers 2, 3, 5, and 6 as more likely to be damaged than the other locations. For the Alabama samples with Colorado reactive aggregates, the crest factors from accelerometer 6 were much higher than at other locations, implying a higher probability of damage in the zone close to accelerometer 6.

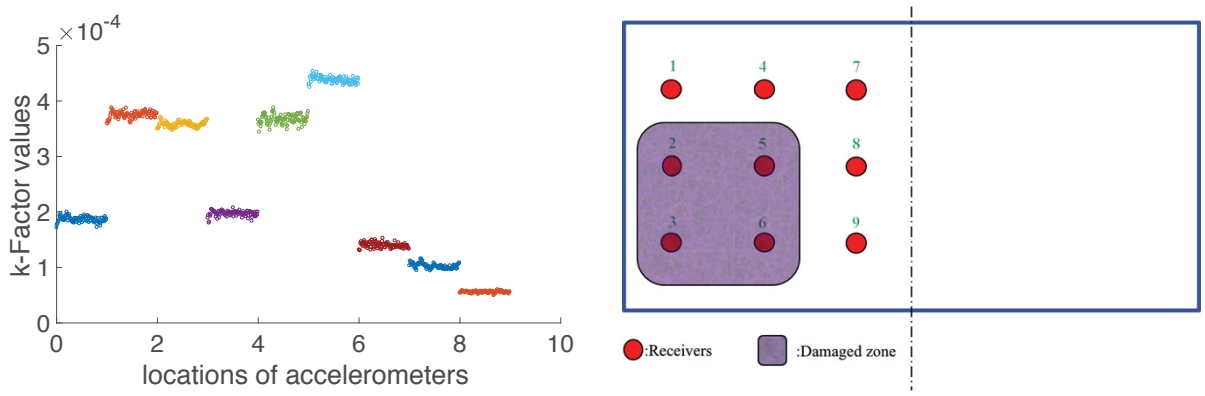

Figure 17. Crest factors for Alabama samples with North Carolina reactive aggregates: (left) direct observation and (right) possibly damaged zone.

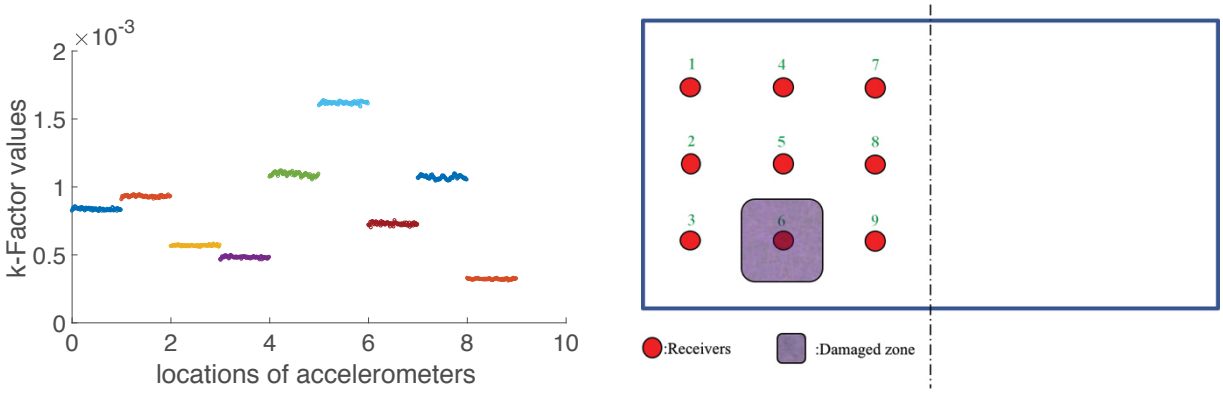

Figure 18. Crest factors for Alabama samples with Colorado reactive aggregates: (left) direct observation and (right) possibly damaged zone.

As an alternative to direct observation, we could also use an unsupervised learning method to cluster the values of the crest factors. Here we use *k*-means clustering to group the candidate locations, based on their damage condition, and set the number of clusters to two. After a hundred iterations of *k*-means clustering, the clustered groups reached a stable result. The results are shown in Figure 19 and Figure 20. The red points indicate the damage cluster, and the blue points indicate the intact cluster. For the reactive Alabama Samples with North Carolina Aggregates, the results from direct observation and the results from *k*-means clustering ($k = 2$) match with each other. For the Alabama Samples with Colorado Aggregates, the results using *k*-means clustering ($k = 2$) are more conservative than the results from direct observations because more locations are identified as damaged. When we apply this method to a relatively large structure, we should expect damage of different kinds and severity, and adjust the number of the clusters accordingly.

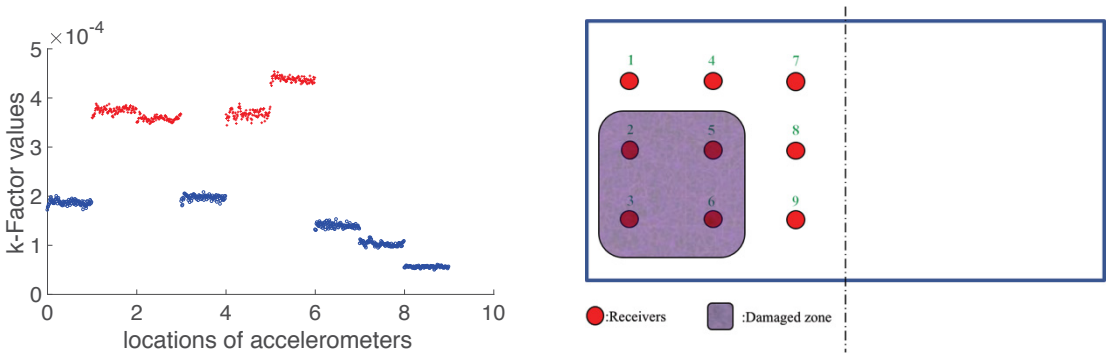

Figure 19. Crest factors for Alabama Samples with North Carolina reactive aggregates: (left) k-means clustering; (right) possible damaged zone.

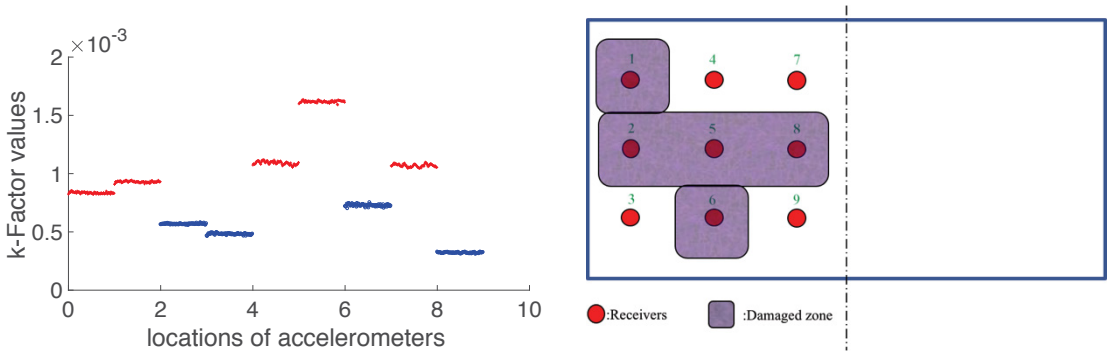

Figure 20. Crest factors for Alabama Samples with Colorado reactive aggregates: (left) *k*-means clustering; (right) possible damaged zone.

We also tested the robustness with 20 different location-selections (as shown in Figure 21) for placing actuator and used a voting-machine scheme to make the decision for damage localization. For demonstration purpose, we did the tests on the left side of Alabama samples with Colorado reactive aggregates. We summarized and normalized the results from these 20 scenarios as a heat map. Red color indicates more percentage votes and blue color indicates less percentage votes as shown in Figure 22.

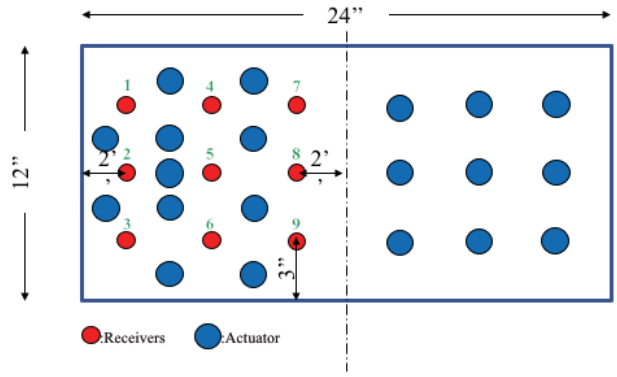

Figure 21. Potential locations showing placement of actuators on the left side of the Alabama slab with Colorado reactive aggregates.

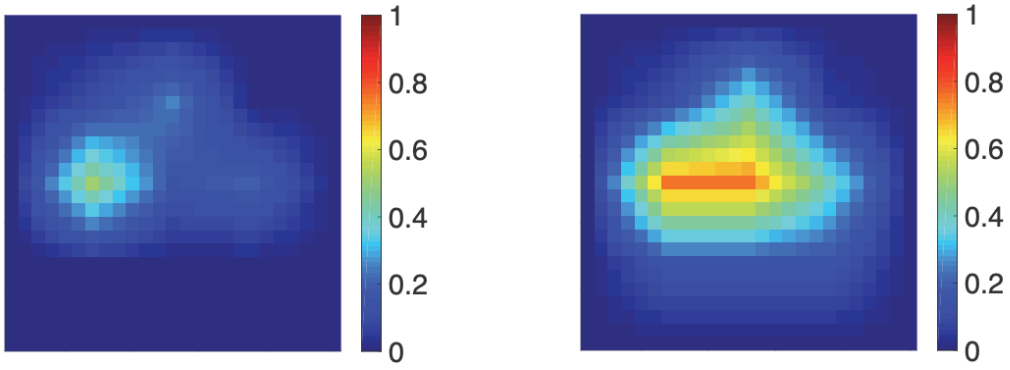

Figure 22. Heat map based on maximum K-Factor value (left) and *k*-means clustering (right).

4. VIBRO-ACOUSTIC TESTING AND RESULTS ON CONCRETE SPECIMENS WITHOUT REINFORCEMENT

4.1 Vibro-acoustic Modulation Results for the Vanderbilt Slab

In this section, we report the results of VAM tests performed on the Vanderbilt University slab. Parameters for this testing are described in Section 2.3.3. The pump and the probe actuators were placed at the center of each quadrant and the center of the slab (as shown in Figure 23), where blue and green circles represent the pump and probe actuators, respectively. We conducted VAM tests using the parameters noted for each quadrant, collected the acceleration time series data at each accelerometer location, computed the corresponding LS, and obtained the SBSum metric. Next, we plotted the variation of the SBSum metric over each quadrant using linear interpolation of the SBSum metric obtained at accelerometer locations. We juxtaposed damage maps for the four quadrants in order to obtain a damage map for the entire slab. Figure 24 and Figure 25 shows damage maps for three probing frequencies.

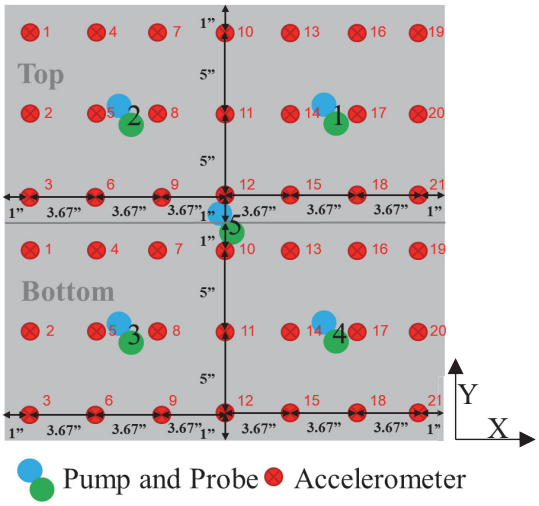

Figure 23. Pump, probe, and accelerometer locations for both halves of the slab (labeled in gray).

The locations of relatively higher SBSum values generally correspond to the locations of visible cracking and effluent seepage in the slab. There is a large crack located between Quadrants 1 and 4. This crack is visible in Figure 25. We also expect a large amount of damage near Quadrants 2, 3, and 4 because there is an area of effluent seepage. This is seen in Figure 24 and Figure 25, where Quadrants 3 and 4 consistently show higher SBSums.

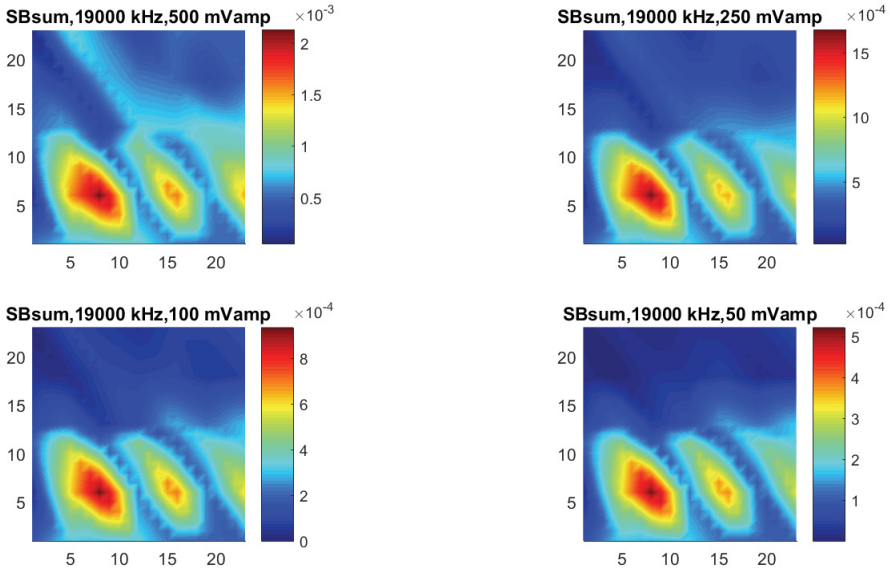

Figure 24. SBSum data in the LS of acceleration given a 500 mV Pump of 920 kHz, and 500, 250, 100, and 50 mV probes of 19 kHz for all five pump and probe locations.

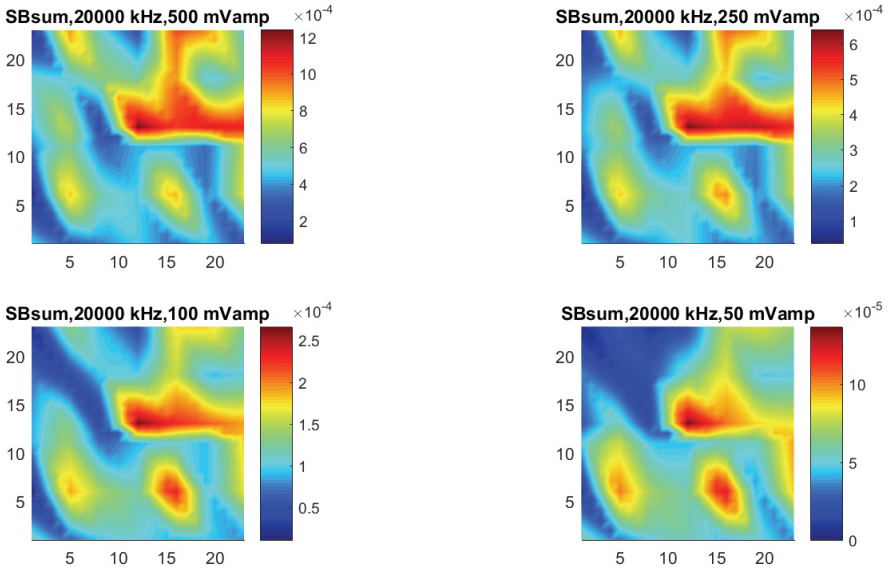

Figure 25. SBSum data in the LS of acceleration given a 500 mV pump of 920 kHz, and 500, 250, 100, and 50 mV probes of 20 kHz for all five pump and probe locations.

4.2 Vibro-acoustic Modulation Results for the Alabama Slabs

In this section, VAM test results are reported for four concrete slabs received from the University of Alabama. Two of the slabs were cast using reactive aggregate, and the remaining two slabs were cast using non-reactive aggregate (see Section 2.2.2). We performed VAM tests and compared the magnitude of damage indices for slabs cast using reactive and non-reactive aggregate. We used a grid of 21 accelerometers for VAM testing of the Alabama slabs. Figure 26 shows locations of accelerometers as

well as pumping and probing actuators. We performed the VAM test, acquired acceleration data for each pump and probe location, computed the damage index (SBSum) using the baseline adjustment method, and summed the damage indices calculated for 10 sets of pump and probe locations. We use linear interpolation to obtain damage index variation (in the form of a damage map) over the top surface of the slab.

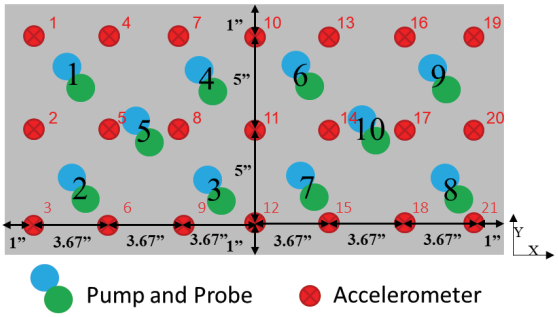

Figure 26. Accelerometer and pump and probe actuators placement for the Alabama samples.

The LS for acceleration shows high-magnitude sidebands for the reactive samples and no sidebands for the control (non-reactive) samples. This simple observation suggests that VAM tests can be used for detection of ASR damage in concrete. The reactive samples show surface cracking, whereas no cracking is observed in control (non-reactive) samples for both North Carolina and Colorado specimens.

We performed damage mapping for the Alabama samples using the method discussed in Section 2.3.4 for calculating the SBSum values. Figure 27 to Figure 30 show damage maps for the pump magnitude of 500 mV pump frequency of 1695 Hz (as specified in Table 2), probe frequency of 19 kHz, and four probe amplitude values (50, 100, 250, and 500 mV). The results for the Colorado reactive (Figure 27) and North Carolina reactive (Figure 29) specimens show a consistent pattern for the distribution of SBSum values for all the four probe amplitudes. The North Carolina and Colorado reactive samples also show consistently high sidebands for the same region for all four probe amplitudes. The results for the reactive samples are more consistent for all probing amplitudes, whereas the control samples (Figure 28 and Figure 30) show no consistency in the values of damage index at a particular region on the slab. The control samples also show lower SBSum values on the surface while large SBSum values are observed along the sides probably due to boundary effect.

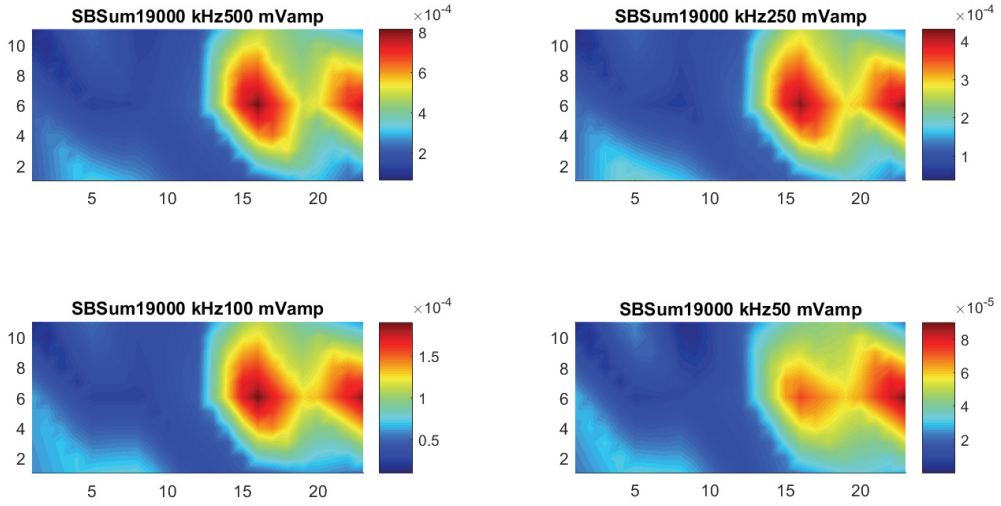

Figure 27. SBSum surface diagram for the Colorado reactive sample with a 1695 Hz and 500 mV pump and a 21 kHz probe of various amplitudes.

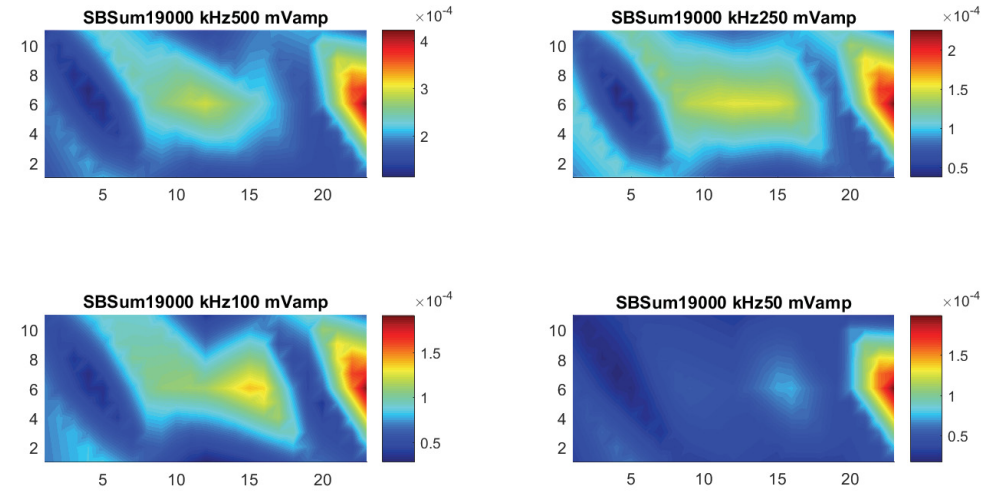

Figure 28. SBSum surface diagram for the Colorado control (non-reactive) sample with a 2240 Hz and 500 mV pump and a 21 kHz probe of various amplitudes.

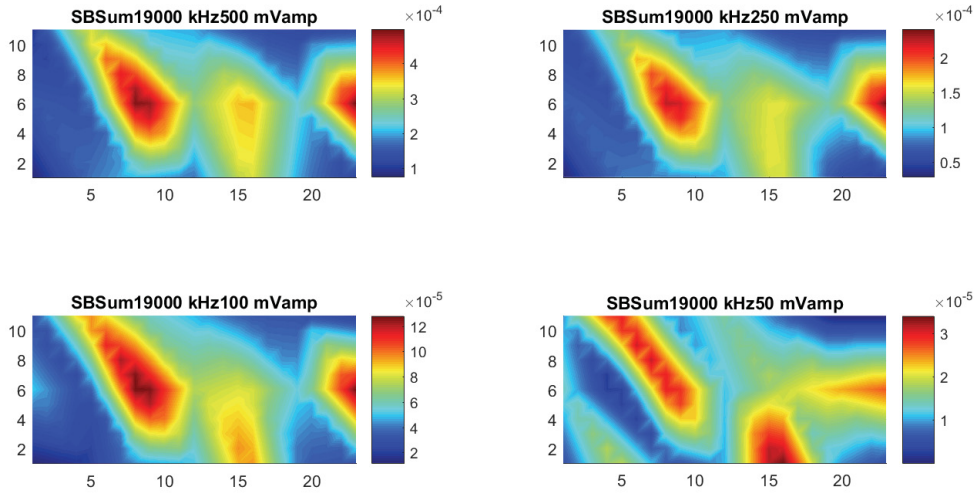

Figure 29. SBSum surface diagram for the North Carolina reactive sample with a 1865 Hz and 500 mV pump and a 19 kHz probe of various amplitudes using a local peak filter.

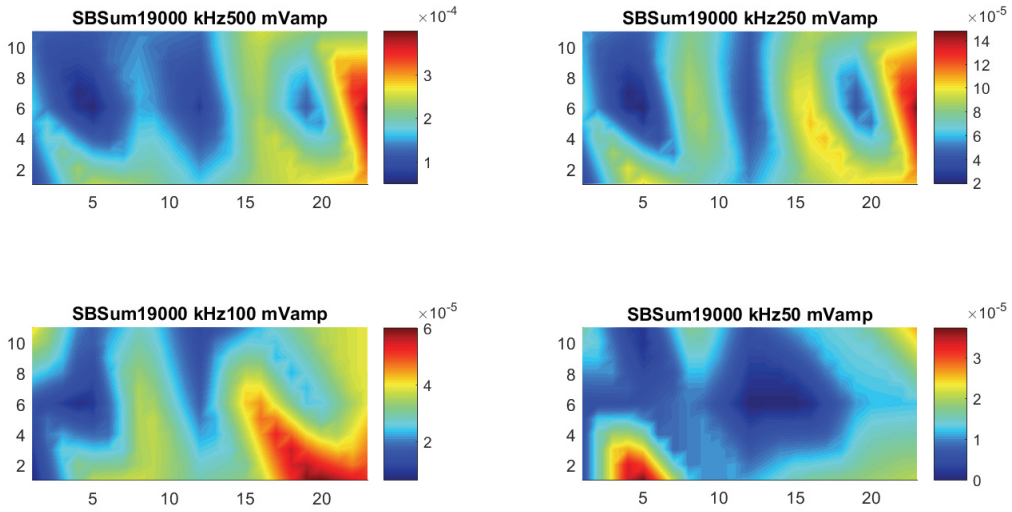

Figure 30. SBSum surface diagram for the North Carolina control (non-reactive) sample with a 2390 Hz and 500 mV pump and a probe of various amplitudes using a local peak filter.

5. DATA-FUSION TECHNIQUES FOR PLAIN CONCRETE VIBRO-ACOUSTIC TESTING DATA

In this section we evaluate different techniques to combine results from multiple VAM experiments. Two main types of fusion techniques were used: averaging and Bayesian fusion. These techniques were applied to raw data and to data converted to a damage index scale.

5.1 Technique Based on Sideband Sum Averaging

One method for evaluating the SBSum data from VAM over multiple experiments with different parameters is by averaging the SBSum results for each accelerometer. Figure 31 shows the average SBSum plot obtained for the Vanderbilt University sample by averaging the values of SBSum at each

sensor over all five different pump and probe locations (as shown in Figure 23). When averaging the results for two different probing frequencies, Figure 31(c), although the overall magnitude decreases, the locations with the highest SBSum values relatively remain the same. Figure 32 looks at the average of the SBSum over all pump and probe configurations as well as the four different probing amplitudes (50, 100, 250, and 500 mV). Although the probing frequency of 15 kHz shows a large value for SBSum for Damage Location 2, it fails to detect the large crack that was seen separating Quadrants 1 and 4.

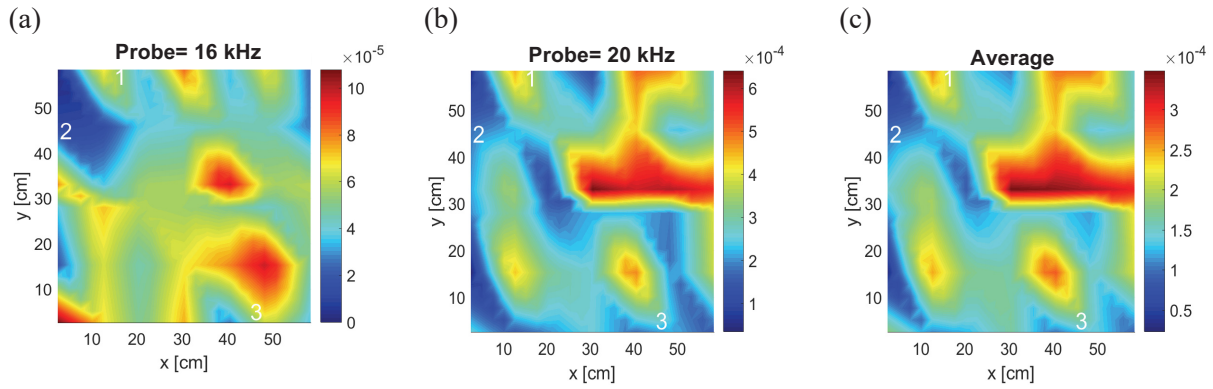

Figure 31. Variation over the average of the SBSum for all five pump and probe configurations of the top surface of the Vanderbilt slab for pump frequency of 920 Hz, and probe amplitude of 250 mV; (a): probe frequency of 16 kHz, (b): probe frequency of 20 kHz, (c): average of results from (a) and (b).

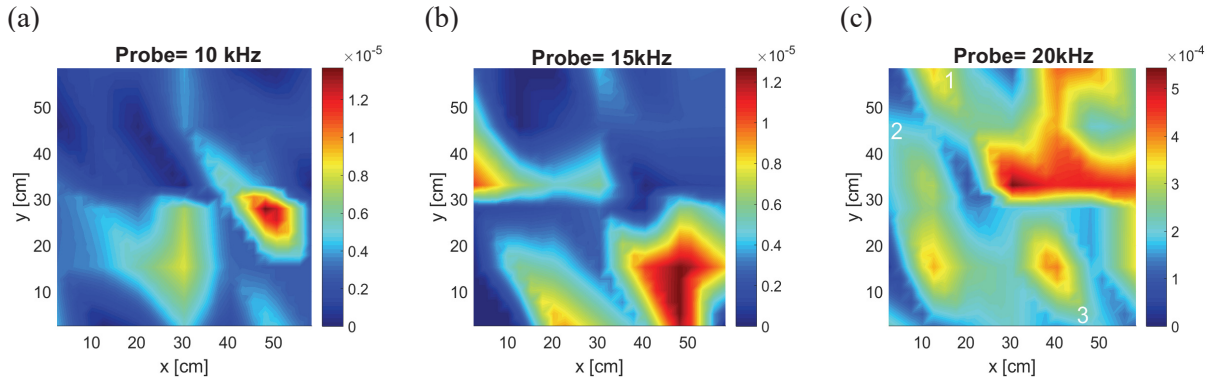

Figure 32. Variation over the average of the SBSum for all five pump and probe configurations and all four probing amplitudes of the top surface of the Vanderbilt slab for pump frequency of 920 Hz; (a): probe frequency of 10 kHz, (b): probe frequency of 15 kHz, (c): probe frequency of 20 kHz.

Another method of fusion using basic averaging methods is, first, to scale each of the experimental results with the maximum SBSum for that given test. This normalizes the data for each experiment and sets the metric values from 0 to 1. The results for Figure 33(a) and Figure 33(b), are the average of normalized data for all five configurations and a probing amplitude of 250 mV. Figure 33(c) is the average of Figure 33(a) and Figure 33(b). These data make it harder to see where the maximum SBSum locations are, but the scale could be altered. Overall, the hypothesized damage locations are very similar to that of Figure 31. In Figure 34, when the value was plotted, it was inferred that the locations with the SBSum were not consistent throughout the averaged experiments, causing the average value to be so low. This was clearly seen when a probing frequency under 16 kHz was used for VAM testing.

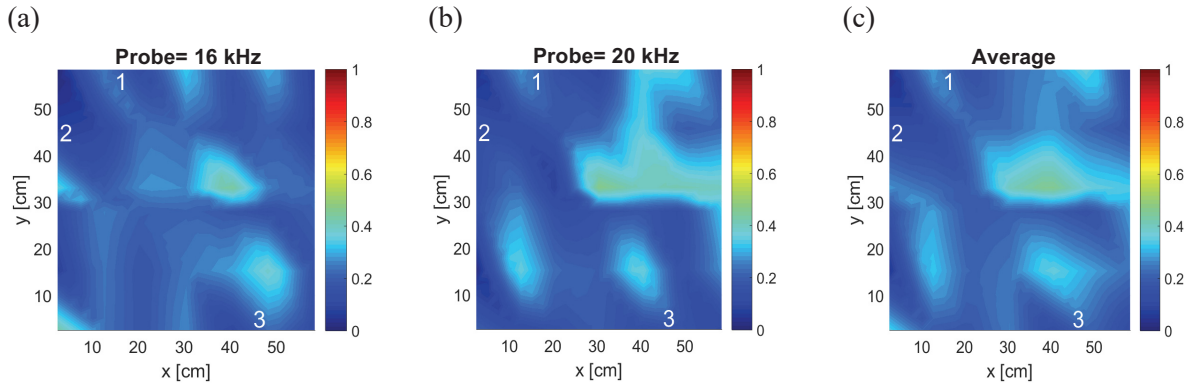

Figure 33. Variation over the average of the scaled SBSum for all five pump and probe configurations of the top surface of the Vanderbilt slab for pump frequency of 920 Hz, and probe amplitude of 250 mV; (a): probe frequency of 16 kHz, (b): probe frequency of 20 kHz, (c): average of results from (a) and (b).

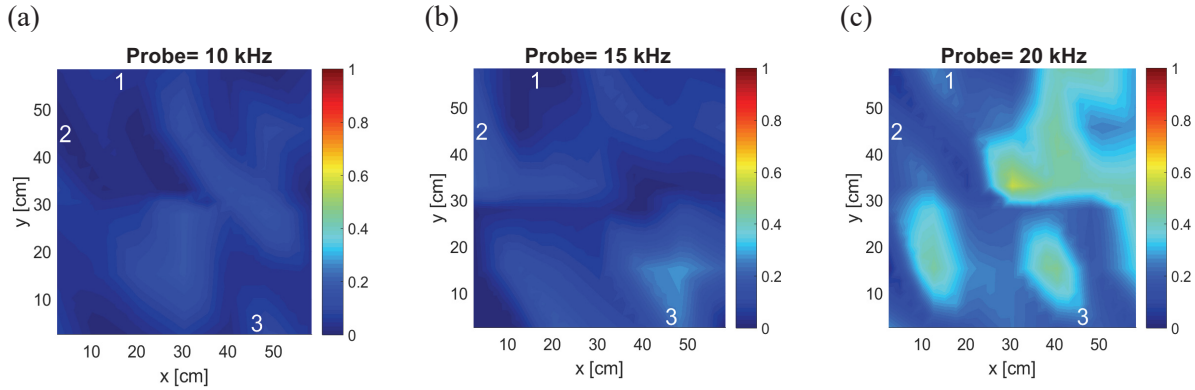

Figure 34. Variation over the average of the scaled SBSum for all five pump and probe configurations and all four probing amplitudes of the top surface of the Vanderbilt slab for pump frequency of 920 Hz; (a): probe frequency of 10 kHz, (b): probe frequency of 15 kHz, (c): probe frequency of 20 kHz.

5.2 Technique Based on Damage Index Averaging

In this section, we convert the SBSum values to damage index values to infer the regions of the specimen that consistently show (relatively) high SBSum values; in other words, these are the regions that are most likely to be near the damaged zone. In a VAM test, sensors showing higher SBSum values (compared to other sensors in the same test) are considered to be the sensors near damage zone. Hence, we define damage index that classifies a given sensor as the one showing or not showing signs of damage. Specifically, we define the damage index at sensor "i", D_i as:

$$D_i = 1 \; if \; SBsum_i \geq \frac{1}{N_{sens}} \sum_i SBsum_i \,, \tag{4}$$

$$= 0 \; otherwise,$$

where N_{sens} denotes the total number of sensors used in a VAM test. Thus, when the SBSum value at a given sensor is higher than the mean SBSum value (for all sensors) for that VAM test, then the sensor is considered to be showing signs of damage.

Results using the damage index are averaged for results using different experimental parameters. In Figure 35(a) and Figure 35(b) are the average of normalized data for all five configurations and a probing amplitude of 250 mV. Figure 35(c) is the average of Figure 35(a) and Figure 35(b). This method works well in retaining information from multiple tests. The results in Figure 35(c) show that there were some sidebands present in the sensor locations near Damage Locations 1, 2, and 3. It also clearly displays a

higher SBSum along the crack between Quadrants 1 and 4. Results for the average of all configurations and probing amplitudes in Figure 36 are similar to results from Figure 34. Probing frequencies below 16 kHz produce results with much smaller SBSum values than the higher frequency results.

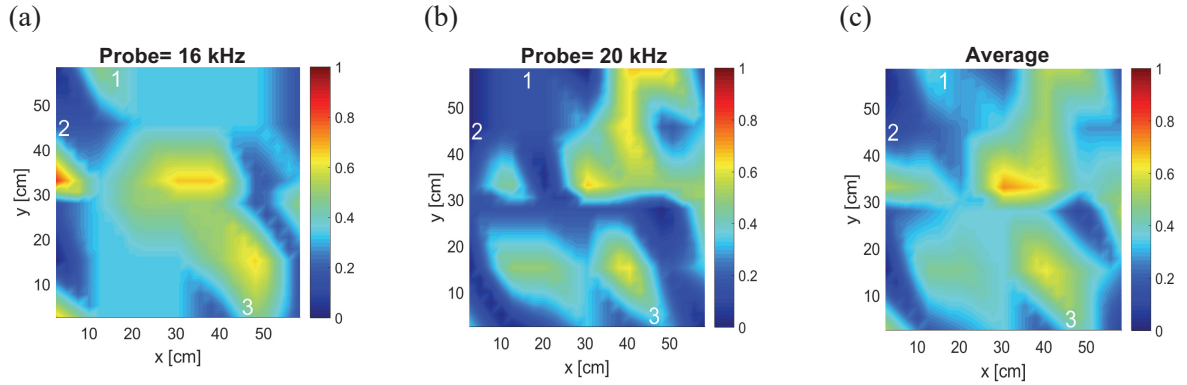

Figure 35. Variation over the average of the damage-index results for all five pump and probe configurations of the top surface of the Vanderbilt slab for pump frequency of 920 Hz, and probe amplitude of 250 mV; (a): probe frequency of 16 kHz, (b): probe frequency of 20 kHz, (c): average of results from (a) and (b).

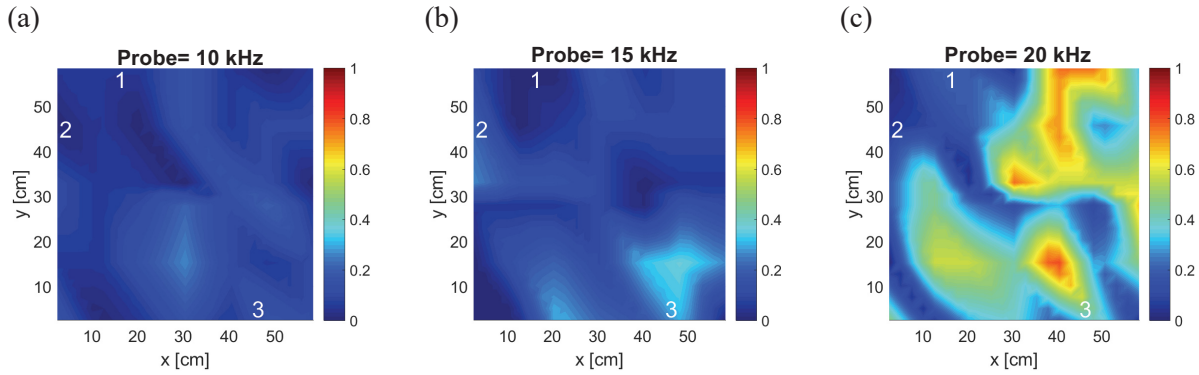

Figure 36. Variation over the average of the damage-index result for all five pump and probe configurations and all four probing amplitudes of the top surface of the Vanderbilt slab for pump frequency of 920 Hz; (a): probe frequency of 10 kHz, (b): probe frequency of 15 kHz, (c): probe frequency of 20 kHz.

5.3 Bayesian Technique for Data Fusion

This section looks at combining the results from multiple VAM experiments by creating a damage probability map using a Bayesian updating technique. For the Bayesian update algorithm, the variable D_i represents the data. It is a discrete random variable with two possible values ($D_i = 1$ or $D_i = 0$). Similarly, we defined a damage parameter at sensor "i" as θ_i. θ_i is a discrete random variable that denotes whether damage is actually present ($\theta_i = 1$), or absent ($\theta_i = 0$) at/near sensor "i". With these definitions in mind, the Bayesian update relation for the damage parameter θ_i at each sensor can be written as:

$$P(\theta_i|D_i) \propto P(D_i|\theta_i) * P(\theta_i)\,, \tag{5}$$

where $P(\theta_i|D_i)$ is the posterior probability mass function (PMF) of variable θ_i, $P(\theta_i)$ is the prior PMF of θ_i, and $P(D_i|\theta_i)$ is the likelihood of observing data ($D_i = 1$ or $D_i = 0$) for a given value of the damage variable ($\theta_i = 1$ or $\theta_i = 0$). Note that in the ideal case, $P(D_i = 1|\theta_i = 1) = 1$, and $P(D_i = 0|\theta_i = 1) = 0$; i.e., the test does not show any false positives or false negatives. However, in real applications, the VAM test suffers from false positives, as well as false negatives. If, for example, an antinode of structural

vibration lies at or near a sensor location, the SBSum value at that sensor may be small, even if it is located near the damaged zone. On the other hand, the wave component corresponding to sideband frequencies may travel away from damage and show up at a sensor located there. Furthermore, measurement noise may create false positive and false negative data (in spite of baseline adjustment and local maxima processing methods). Thus, it is necessary to evaluate the sensitivity and specificity of VAM tests for thick elastic media containing breathing cracks. This is typically done using numerical simulation of the test procedure. In a numerical VAM test, the value of the damage parameter (θ_i) is known, and the value of the damage index can be computed using the recorded dynamic response (displacement time history). For the experiments reported in this report, numerical simulation of VAM tests implies modeling nonlinear wave propagation in concrete specimens and blocks containing cracks for multiple crack locations, pump and probe amplitudes, and probe frequencies. Modeling wave propagation in heterogeneous media like concrete (with cement and randomly distributed aggregate) is a computationally challenging task. Thus, we neglect the material heterogeneity, and simulate wave propagation in a homogeneous elastic specimen with concrete-like properties. Even with this simplifying assumption, simulation of nonlinear wave propagation in three-dimensional media is computationally expensive. The geometric nonlinearity at the crack interface necessitates employment of an implicit time-integration scheme for the simulations, which increases the computational burden significantly. To overcome this difficulty, we modeled the wave propagation in a two-dimensional specimen, under plane strain assumptions. Our previous work indicated that this model is suitable for computing the sensitivity and specificity for VAM tests with different test parameters as well as measurement noise. The domain geometry, the crack locations, and the pump and probe locations used in our numerical simulations are shown in Figure 37. The computational domain is 60.96 cm wide and 15.24 cm thick. It contains a crack of length 12.7 cm at mid-thickness (7.62 cm from the top surface). We used a commercial finite-element program (Abaqus) to perform numerical simulation. We discretized the domain using a structured mesh of 8-noded finite elements. We employed an implicit scheme for time integration of governing equations, and ensure that at least 10 computational nodes are available over the smallest wavelength. We modeled the interaction at the crack interface using a hard, frictionless contact condition. The material properties used in our simulations are given in Table 3.

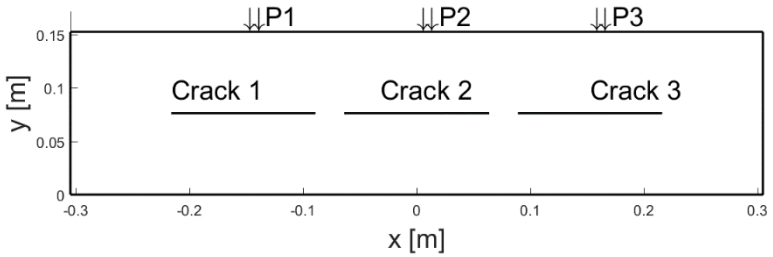

Figure 37. Two-dimensional domain showing crack locations and pump/probe locations (P1, P2, P3) used for likelihood computation.

Table 3. Material properties used in numerical simulation for likelihood computation.

Material property	**Value**
Young's modulus (E)	27 GPa
Density (ρ)	0.15
Poisson's ratio (ν)	2400 kg/m^3
Mass proportional Rayleigh damping parameter (a)	2120.04
Stiffness proportional Rayleigh damping parameter (b)	1.787×10^{-7}

We simulated the nonlinear wave propagation for different combinations of pump and probe locations, crack locations, probe frequency and probe and pump amplitude ratios (Amp_{probe} / Amp_{pump}). We recorded the time history of displacements on the top surface at all computational nodes. We computed the SBSum metric and the damage index for all nodes. In a given simulation, the nodes located directly above the crack are the nodes for which the damage parameter value is 1 (θ_i = 1), otherwise θ_i = 0. Thus, we knew the truth about the damage parameter, and we computed the damage index (D_i) at each computational node. In this manner, we arrived at false positives and false-negative results at each node for each numerical VAM test. For example, the true/false positive/negative values for pump and probe located at P2, Crack 1, $f_{pu} = 1$ kHz, $f_{pr} = 15$ kHz, and Amp_{probe} / Amp_{pump} = 0.1 are shown in Figure 38.

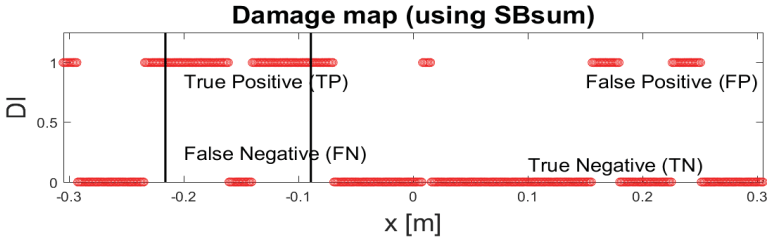

Figure 38. VAM test results for pump/probe located at P2, crack 1, $f_{pu} = 1$ kHz, $f_{pr} = 15$ kHz, and Amp_{probe} / Amp_{pump} = 0.1.

The matrix of VAM test parameters used in our numerical simulations are given in Table 4.

Table 4. VAM test parameters used for likelihood computation.

Variable	Values
Crack location	Crack 1, Crack 2, Crack 3 (see Figure 37)
Probe frequency (Hz)	10000, 12000, 14000, 16000, 18000, 20000
Amp_{probe}/Amp_{pump}	1, 0.5, 0.2, 0.1
Pump/probe location	P1, P2, P3 (see Figure 37)

In this manner, we compute the D_i values for known θ_i values for 216 VAM tests with different test parameters and crack locations. We count the false positives, false negatives, true positives, and true negatives for these tests to arrive at the following (approximate) values for the likelihood function:

$$P(D_i = 1|\theta_i = 1) = 0.653 \quad (6)$$

$$P(D_i = 0|\theta_i = 1) = 0.338 \quad (7)$$

$$P(D_i = 1|\theta_i = 0) = 0.347 \quad (8)$$

$$P(D_i = 0|\theta_i = 0) = 0.662 \quad (9)$$

We use these likelihood values and the following Bayesian update equations for data fusion:

$$P(\theta_i = 1|D_i = 1) = \frac{P(D_i = 1|\theta_i = 1)*P(\theta_i=1)}{P(D_i = 1|\theta_i = 1)*P(\theta_i=1)+P(D_i = 1|\theta_i = 0)*P(\theta_i=0)} \quad (10)$$

$$P(\theta_i = 1|D_i = 0) = \frac{P(D_i = 0|\theta_i = 1)*P(\theta_i=1)}{P(D_i = 0|\theta_i = 1)*P(\theta_i=1)+P(D_i = 0|\theta_i = 0)*P(\theta_i=0)} \quad (11)$$

For the first update, we start with uniformed prior ($P(\theta_i = 1) = P(\theta_i = 0) = 0.5$), and update the damage parameter at each sensor location using the experimental data for the first VAM laboratory test.

For the second (and subsequent) updates, we use the posterior from the first (previous) update as the prior and obtain posterior using the equations given above.

Figure 39 used the Bayesian-fusion method to combine results from all five configurations of the pump and probe, using a stated probing frequency of 16 and 20 kHz and a probing amplitude of 250 mV. Figure 39(c) is the Bayesian fusion of Figure 39(a) and Figure 39(b). Figure 40 is the average of all configurations and probing amplitudes for different probing frequencies. These results make it very clear that results using a probing amplitude less than 16 kHz give very little input on damage localization.

Figure 39 and Figure 40 show much clearer results for damage probability using the assumed likelihood values. The current issue with this technique is that the likelihood values are an approximation using a two-dimensional numerical model, which could skew our results if it is far off from the true value.

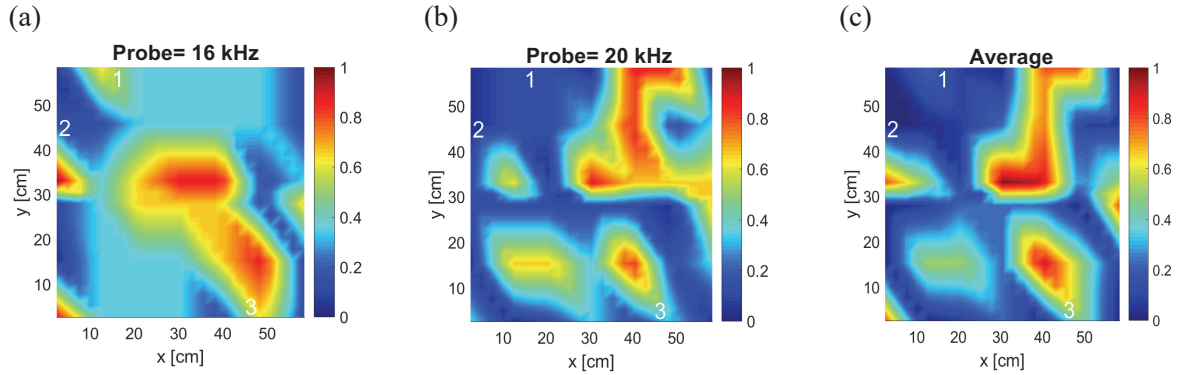

Figure 39. Bayesian-fusion results for all five pump and probe configurations of the top surface of the Vanderbilt slab for pump frequency of 920 Hz, and probe amplitude of 250 mV; (a): probe frequency of 16 kHz, (b): probe frequency of 20 kHz, (c): fusion of results from (a) and (b) using Bayesian-fusion.

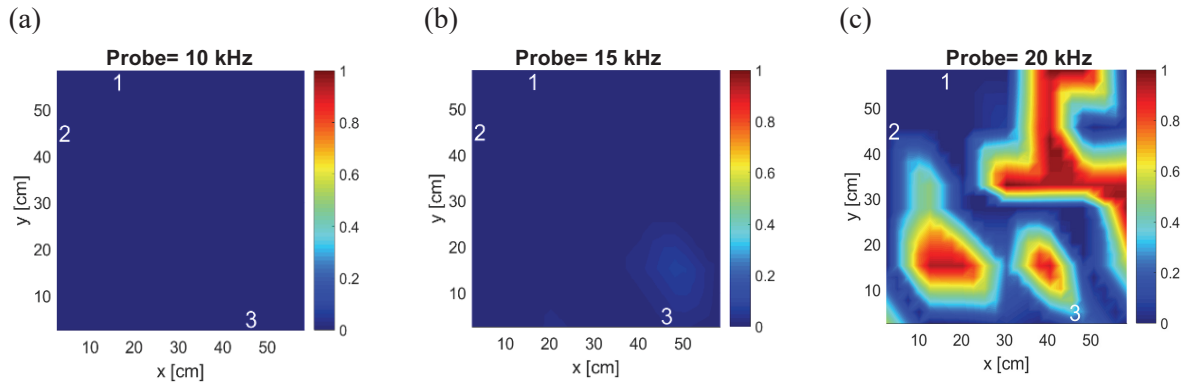

Figure 40. Bayesian fusion of the result for all five pump and probe configurations and all four probing amplitudes of the top surface of the Vanderbilt slab for pump frequency of 920 Hz; (a): probe frequency of 10 kHz, (b): probe frequency of 15 kHz, (c): probe frequency of 20 kHz.

It is difficult to determine which fusion technique is best for damage localization or whether any technique should be used. In the Bayesian-fusion technique, some results are overpowered by others causing it to appear as though the top right quadrant of the Vanderbilt sample showed no SBSum results. The averaging technique still displayed some of this information regarding the SBSum in that location when fusing different results. Validating the damage locations by running petrography on different cored locations to determine the locations of ASR allows us to determine which technique was best.

6. VIBRO-ACOUSTIC TESTING AND RESTULTS OF CONCRETE SPECIMENS WITH REINFORCEMENT

In this section, VAM test results are reported for four concrete slabs received from the University of Nebraska-Lincoln. We performed VAM tests and compare the magnitude of damage indices for slabs cast using reactive and non-reactive aggregate. We used a grid of 21 accelerometers for VAM testing of the Nebraska slabs. Figure 41 shows locations of accelerometers as well as pumping and probing actuators. We performed the VAM test, acquired acceleration data for each pump and probe location, computed the damage index (SBSum) using the baseline adjustment method, maximum local peaks, and summed the damage indices calculated for 10 sets of pump and probe locations. We used linear interpolation to obtain damage-index variation (i.e., a damage map) over the top surface of the slab.

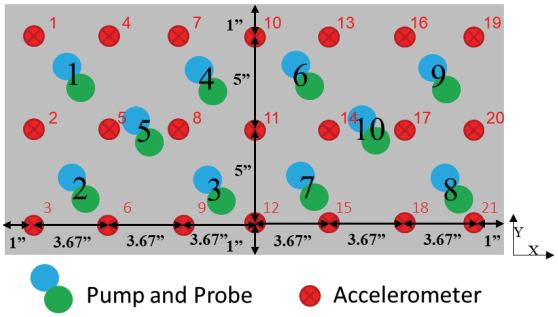

Figure 41. Accelerometer and pump and probe actuators placement for the Nebraska samples.

The LS for acceleration showed high-magnitude sidebands for the reactive samples and no sidebands for the control (non-reactive) samples. Probing frequencies used were the approximate first modal frequency taken at the first period of testing, 28 days after the specimens were cast, as displayed in Table 5.

Table 5. Experimental first modal frequency for each Nebraska sample.

Slab Sample	Approximate First Modal Frequency (Hz)
Control	2375
ASR Non-Reinforced	2445
ASR 1-D	2140
ASR 2-D	2335

6.1 Analysis of Vibro-acoustic Modulation Data

This section shows the VAM results for the Nebraska samples at different parameter inputs for three different time periods with at least 6 weeks of aggressive curing in between collections.

VAM results for the control sample are displayed in Figure 42 and Figure 43. Both tests had a pumping frequency of 2375 Hz and pumping amplitude of 500 mV. Figure 42 is for Configuration 6, with a probing frequency of 20 kHz and amplitude of 250 mV. Figure 43 is for Configuration 1, with a probe frequency of 18 kHz and probe amplitude of 500 mV. The SBSum values for this slab are not consistent between experiments, and there are no sidebands. We conclude that this slab does not display any ASR damage.

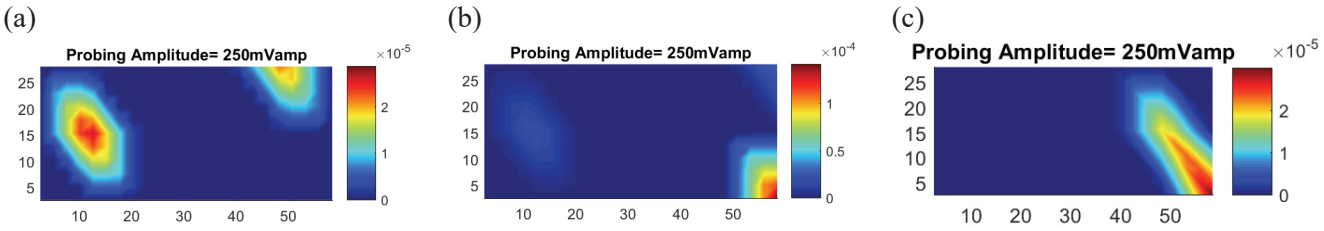

Figure 42. SBSum results for the control specimen with a pumping frequency of 2375 Hz at an amplitude of 500 mV, a probing frequency of 20 kHz at an amplitude of 250 mV, and pump and probe at Configuration 6. (a) Data collected on Nov. 5, 2018, (b) data collected on Jan. 15, 2019, and (c) data collected on Mar. 4, 2019.

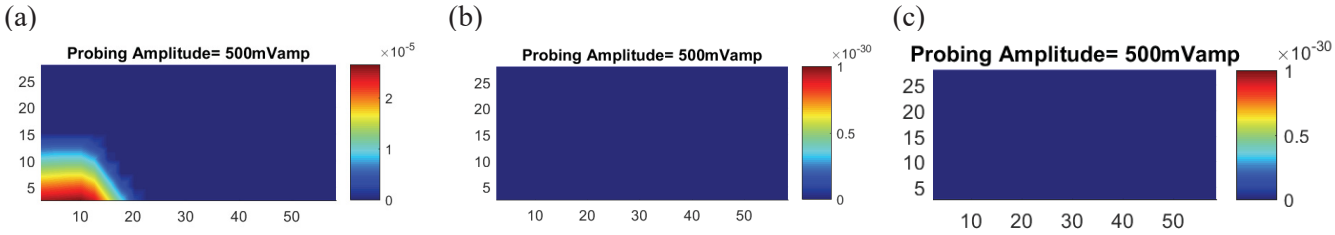

Figure 43. SBSum results for the control specimen with a pumping frequency of 2375 Hz at an amplitude of 500 mV, a probing frequency of 18 kHz at an amplitude of 500 mV, and pump and probe at Configuration 1. (a) Data collected on Nov. 5, 2018, (b) data collected on Jan. 15, 2019, and (c) data collected on Mar. 4, 2019.

VAM results for the ASR non-reinforced specimen are displayed in Figure 44 and Figure 45. Both tests have a pumping frequency of 2445 Hz and pumping amplitude of 500 mV. Figure 44 is for Configuration 5, with a probing frequency of 21 kHz and amplitude of 250 mV. Figure 45 is for Configuration 7, with a probe frequency of 20 kHz and probe amplitude of 500 mV. For both VAM tests, there appears to be no consistent area of increased SBSum for the tests conducted in November and January (Figure 44(a)-(b) and Figure 45(a)-(b)). In the tests taken in March (Figure 44(c) and Figure 45(c)) there appears to be an increased value for SBSum near Accelerometers 8, 12, 14, and 15. It is likely ASR has started to form in the specimen in this region after the 12 weeks of aggressive curing.

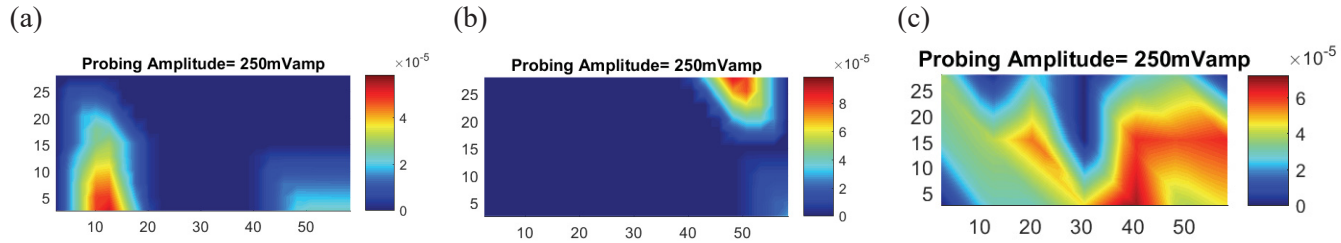

Figure 44. SBSum results for the ASR non-reinforced specimen with a pumping frequency of 2445 Hz at an amplitude of 500 mV, a probing frequency of 21 kHz at an amplitude of 250 mV, and pump and probe at Configuration 5. (a) Data collected on Nov. 5, 2018, (b) data collected on Jan. 15, 2019, and (c) data collected on Mar. 4, 2019.

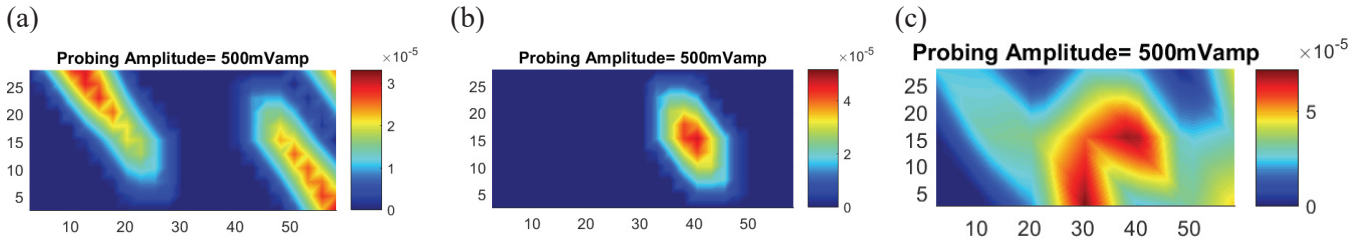

Figure 45. SBSum results for the ASR non-reinforced specimen with a pumping frequency of 2445 Hz at an amplitude of 500 mV, a probing frequency of 20 kHz at an amplitude of 500 mV, and pump and probe at Configuration 7. (a) Data collected on Nov. 5, 2018, (b) data Collected on Jan. 15, 2019, and (c) data collected on Mar. 4, 2019.

VAM results for the ASR specimen reinforced in one direction (1-D) are displayed in Figure 46 and Figure 47. Both tests have a pumping frequency of 2140 Hz and pumping amplitude of 500 mV. Figure 46 is for Configuration 9, with a probing frequency of 18 kHz and amplitude of 100 mV. Figure 47 is for Configuration 3, with a probe frequency of 20 kHz and probe amplitude of 250 mV. For both VAM tests there appears to be no consistent area of increased SBSum for the tests conducted in November, January, and March (Figure 46(a)-(c) and Figure 47(a)-(c)). Rebar in this block is located underneath Accelerometers 4, 5, 6, 16, 17, and 18. In Figure 47(c), Accelerometers 16, 17, and 18 show a large SBSum value. This is likely due to delamination around the rebar. It is also possible ASR could form along the rebar and even fill the delamination location.

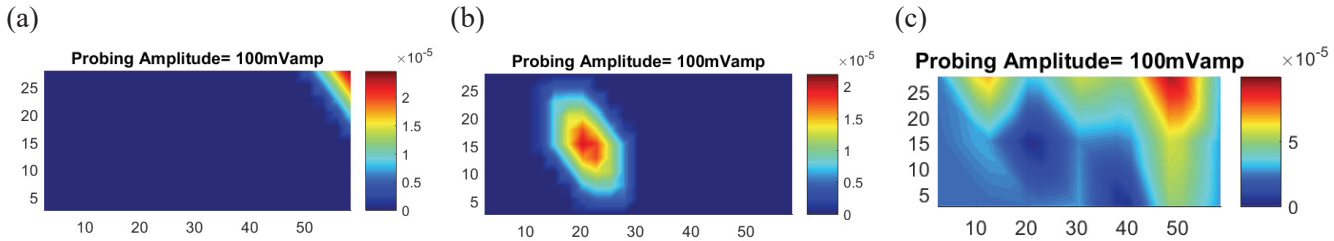

Figure 46. SBSum results for the ASR 1-D specimen with a pumping frequency of 2140 Hz at an amplitude of 500 mV, a probing frequency of 18 kHz at an amplitude of 100 mV, and pump and probe at Configuration 9. (a) Data collected on Nov. 5, 2018, (b) data collected on Jan. 15, 2019, and (c) data collected on Mar. 4, 2019.

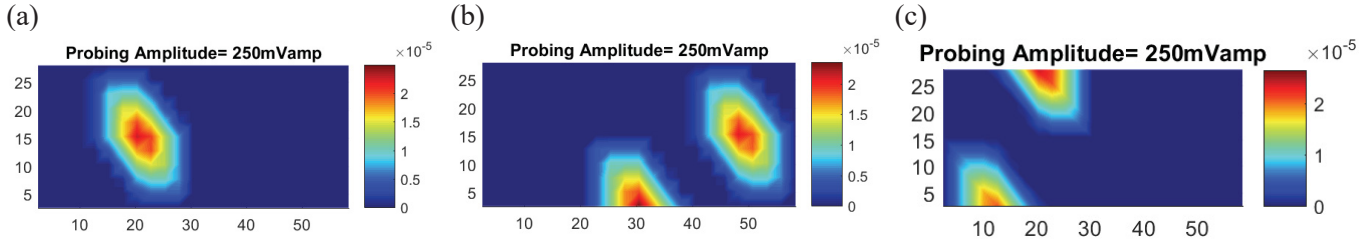

Figure 47. SBSum results for the ASR 1-D specimen with a pumping frequency of 2140 Hz at an amplitude of 500 mV, a probing frequency of 20 kHz at an amplitude of 250 mV, and pump and probe at Configuration 3. (a) Data collected on Nov. 5, 2018, (b) data collected on Jan. 15, 2019, and (c) data collected on Mar. 4, 2019.

Figure 48 and Figure 49 show SBSum results for the ASR specimen reinforce in two directions (2-D). Figure 48 and Figure 49 shows results for VAM experiments at Configuration 7, with a probing amplitude of 250 mV and a pumping frequency of 2335 Hz and 500 mV amplitude. Figure 48 is for a probing frequency of 20 kHz, and Figure 49 is for a probing frequency of 19 Hz. In the first VAM test for

the 20 kHz case (Figure 48(a)), there is some noise in the center-right portion of the slab. Further analysis of LS plots shows that this noise does not appear to be sidebands, but it is unclear what is causing it. In the consecutive testing, Figure 48(b) and Figure 48(c), there are sidebands present at Accelerometer 14, which cause the SBSum to be much higher. For the VAM tests using the 19 kHz probing frequency, there appear to be no sidebands in that region for the first two tests (Figure 49(a)-(b)) but sidebands appear in the Accelerometer 14 region for the most recent set of experiments (Figure 49(c)). This increase in the SBSum in this region could be due to ASR or rebar delamination since the first set of tests showed some excitement in this region as well.

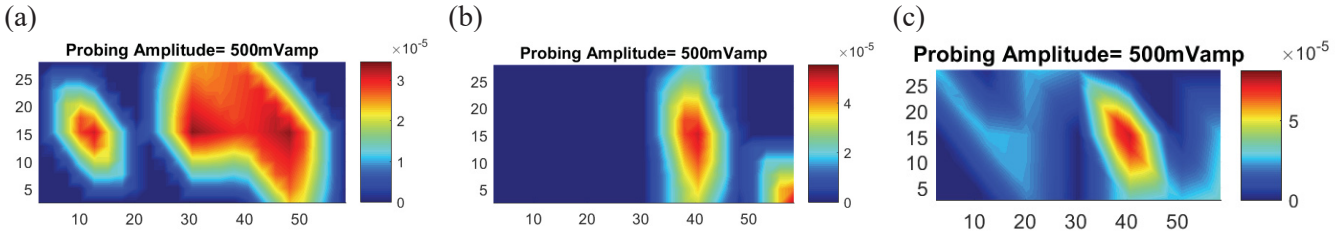

Figure 48. SBSum results for the ASR 2-D specimen with a pumping frequency of 2335 Hz at an amplitude of 500 mV, a probing frequency of 20 kHz at an amplitude of 500 mV, and pump and probe at Configuration 7. (a) Data collected on Nov. 5, 2018, (b) data collected on Jan. 15, 2019, and (c) data collected on Mar. 4, 2019.

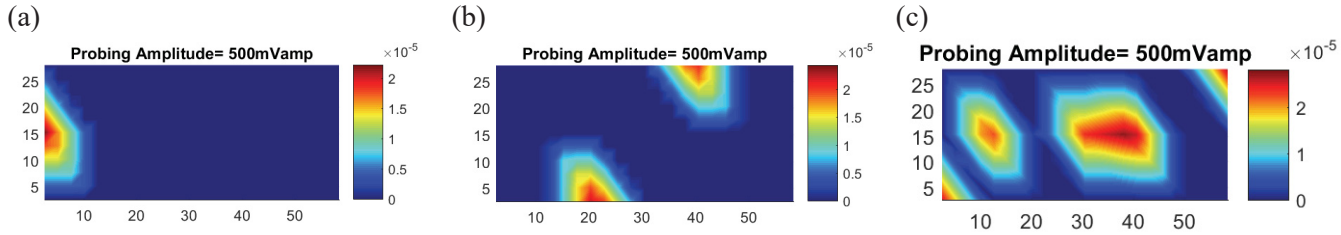

Figure 49: SBSum results for the ASR 2-D specimen with a pumping frequency of 2335 Hz at an amplitude of 500 mV, a probing frequency of 19 kHz at an amplitude of 500 mV, and pump and probe at Configuration 7. (a) Data collected on Nov. 5, 2018, (b) data collected on Jan. 15, 2019, and (c) data collected on Mar. 4, 2019.

In the analysis of the VAM tests conduction on the Nebraska specimens, the presence of rebar does not seem to have affected the initial VAM results; however, it is difficult to determine whether the increase in SBSum in later experiments is due to delamination around the rebar or due to ASR damage. It is important to monitor these areas further to see whether the damage spreads into other regions. VAM results can also be compared to mechanical expansion calculations to see if ASR could be causing the specimens to expand.

7. SUMMARY AND FUTURE WORK

The objectives of this report were to examine the application of vibration-based techniques in ASR damage diagnosis and to develop approaches for uncertainty quantification in diagnosis. The vibration-based techniques were applied to a 24 in. × 24 in. × 6 in. slab cast at Vanderbilt University with four pockets of reactive aggregates, four 24 in. × 12 in. × 12 in. slabs with reactive and non-reactive aggregates (dispersed throughout the slabs) from the University of Alabama, and four 24 in. × 12 in. × 12 in. slabs with reactive and non-reactive aggregates, reinforced and non-reinforced, from the University of Nebraska–Lincoln. The main outcomes of the experiments and subsequent analyses include:

1. Both vibration-based techniques detected and localized the damage in the medium-sized concrete slabs from both Vanderbilt and Alabama. In VAM testing, the occurrence of sidebands is dependent

on the pumping and probing actuator locations, the two excitation amplitudes, and the two excitation frequencies.

2. The vibration test results can be fused using voting, averaging, or Bayesian-fusion techniques to synthesize the results given different testing parameters.
3. The single- and dual-frequency vibration tests show similar results for damage localization in the Alabama specimens. For the Vanderbilt specimen, different actuator locations indicate different damage regions in the slab; however, the fusion appears to eliminate some of these regions.
4. The presence of steel reinforcement did not affect the initial VAM test results of the reinforced concrete specimens from the University of Nebraska–Lincoln. No sidebands were observed in the initial testing conducted in November 2018.

Future work should focus on the following issues:

1. The vibration techniques have in general shown good performance in terms of identifying the damage locations. Future work needs to focus on scaling up and automating the technique to large-scale field implementation for damage diagnosis in NPP concrete structures. One of the key challenges is the number of sensors (accelerometers) needed. For a large structure, it is not feasible to use a large number of accelerometers; therefore, a remote-sensing, full-field observation technique (such as laser vibrometry) might be beneficial.
2. Validation of VAM to detect ASR is important to help improve the technique and decrease the uncertainty of damage locations. Four cores were taken from the Vanderbilt sample and shipped to be analyzed using petrography. These data can next be used to help optimize testing parameters and fusion techniques. Cores from other specimens should be obtain similarly and subject to petrographic tests to confirm the presence of ASR damage.
3. Scaling VAM to realistic applications also requires the combination of computational modeling with experiments to further improve damage localization. A related issue is the effect of uncertainty in diagnosis and prognosis due to sensor noise, model uncertainty, and many other sources of concrete variability.
4. The uncertainty quantification methodology presented in this report was applied to VAM-based diagnosis and prognosis. However, the methodology is general and is capable of being applied to multiple techniques that collect spatially distributed data. Future work needs to investigate the incorporation of uncertainty quantification in developing a robust prognostics and health management framework.

8. REFERENCES

Agarwal, V. and S. Mahadevan, 2014, "Concrete Structural Health Monitoring in Nuclear Power Plants," *Office of Nuclear Energy Sensors and Instrumentation Newsletter*, September 2014.

ASTM C1293-08b, 2015, "Standard Test Method for Determination of Length Change of Concrete due to Alkali-Silica Reaction," ASTM International, August 2015.

ASTM C1567-13, 2013, "Standard Test Method for Determining the Potential Alkali-Silica Reactivity of Combinations of Cementitious Materials and Aggregate (Accelerated Mortar-Bar Method)," ASTM International, 2013.

Bao, Y. and S. Mahadevan, 2018, "Harmonic vibration testing for damage detection and localization in concrete," *Structural Health Monitoring*, p.1475921718816837.

Bruck, P., T. Esselman, and M. Fallin, 2012, "Digital Image Correlation for Nuclear," *Nuclear Engineering International*, April 23, 2012.

Chen, J., A. R. Jayapalan, J.-Y. Kim, K. E. Kurtis, and L. J. Jacobs, 2009, "Nonlinear wave modulation spectroscopy method for ultra-accelerated alkali-silica reaction assessment," *ACI Materials Journal*, Vol. 106, pp. 340–348.

Chen, X. J., J.-Y. Kim, K. E. Kurtis, J. Qu, C. W. Shen, and L. J. Jacobs, 2008, "Characterization of progressive microcracking in Portland cement mortar using nonlinear ultrasonics," *NDT&E International*, Vol. 41, pp. 112–118.

Christensen, J. A., 1990, "NPAR Approach to Controlling Aging in Nuclear Power Plants," *Proceedings of the 17th Water Reactor Safety Information Meeting*, Washington, D.C., NUREG/CP-0105, Vol. 3, pp. 509–529.

Kim, S., D. E. Adams, H., Sohn, G. Rodriguez-Rivera, N. Myrent, R. Bond, J. Vitek, S. Carr, A. Grama, and J. J. Meyer, 2014, "Crack detection technique for operating wind turbine blades using Vibro-Acoustic Modulation," *Structural Health Monitoring*, Vol. 13, No. 6, pp. 660–670.

Kreitman, K., 2011, "Nondestructive Evaluation of Reinforced Concrete Structures Affected by Alkali-Silica Reaction and Delayed Ettringite Formation," M.S. Thesis: University of Texas at Austin, Austin, Texas.

Lapedes, A. S., and R. M. Farber, 1988, "How neural nets work," in *Neural information processing systems*, pp. 442-456.

Mahadevan, S., V. Agarwal, K. Neal, D. Kosson, and D. Adams, 2014, *Interim Report on Concrete Degradation Mechanisms and Online Monitoring Techniques*, INL/EXT-14-33134, Idaho National Laboratory, September 2014.

Mahadevan, S., V. Agarwal, K. Neal, P. Nath, Y. Bao, G. Cai, P. Orme, D. Adams, and D. Kosson, 2016, *A Demonstration of Concrete Structural Health Monitoring Framework for Degradation due to Alkali-Silica Reaction*, INL/EXT-16-38602, Idaho National Laboratory, April 2016.

Mahadevan, S., S. Miele, K. Neal, Y. Bao, V. Agarwal, B. T. Pham, D. Adams, and D. Kosson, 2017, *Interrogation of Alkali-Silica Reaction Degraded Concrete Samples using Acoustic and Thermal Techniques to Support Development of a Structural Health Monitoring Framework*, INL/EXT-17-41852, Idaho National Laboratory, April 2017.

Mahadevan, S., S. Miele, P. Karve, J. Frinfrock, V. Agarwal, E. Giannini, 2018, *Enhancement of the Structural Health Monitoring Framework by Optimizing Vibro-Acoustic Modulation Techniques to Localize Alkali-Silica Reaction Degradation in Medium-Sized Concrete Samples*, INL/EXT-18-45212, Idaho National Laboratory, April 2018.

Naus, D., 2007, "Activities in Support of Continuing the Service of Nuclear Power Plant Safety-Related Concrete Structures," in *Infrastructure Systems for Nuclear Energy,* T. T. C. Hsu, C.-L. Wu, and J.-L. Li (eds), Chichester, United Kingdom: John Wiley & Sons, Ltd.

Neal, K., S. Mahadevan, V. Agarwal, G. Thorne, D. Koester, and B. T. Pham, 2016, *Digital Image Correlation of Concrete Slab at University of Tennessee, Knoxville*, INL/EXT-16-39921, Idaho National Laboratory, September 2016.

NextEra Energy Seabrook, 2012, "Impact of Alkali-Silica Reaction on Concrete Structures and Attachments," the Response to Confirmatory Action Letter, SBK-L-12106, from NextEra Energy Seabrook to the Nuclear Regulatory Commission (NRC), May 24, 2012.

Nuttall, Albert H. "Some Windows with Very Good Sidelobe Behavior." *IEEE Transactions on Acoustics, Speech, and Signal Processing* Vol. ASSP-29, February 1981, pp. 84–91.

Singh, A. K., B. Chen, V.B. Tan, T. E. Tay, & H.P. Lee, 2017, “A theoretical and numerical study on the mechanics of vibro-acoustic modulation,” *The Journal of the Acoustical Society of America*, Vol. 141, No. 4, pp. 2821–2831.

Sobol, I.M. “Global sensitivity indices for nonlinear mathematical models and their Monte Carlo estimates,” *Mathematics and Computers in Simulation*, Vol. 55, No. 1–3, pp. 271–280, 2001.

Ulm, F. J., O. Coussy, L. Kefei, and C. Larive, 2000, “Thermo-chemo-mechanics of ASR expansion in concrete structures,” *Journal of Engineering Mechanics*, Vol. 126, No. 3, pp. 233–242.

Welch, P. D. (1967), "The use of Fast Fourier Transform for the estimation of power spectra: A method based on time averaging over short, modified periodograms", *IEEE Transactions on Audio and Electroacoustics*, Vol. AU-15, No. 2, pp. 70–73.